

NOISE-BASED DETECTION AND SEGMENTATION OF NEBULOUS OBJECTS

MOHAMMAD AKHLAGHI, AND TAKASHI ICHIKAWA

Astronomical Institute, Tohoku University, Aoba, Sendai 980-8578, Japan; akhlaghi@astr.tohoku.ac.jp

Received 2014 November 17; accepted 2015 April 6; published 2015 August 26

ABSTRACT

A noise-based non-parametric technique for detecting nebulous objects, for example, irregular or clumpy galaxies, and their structure in noise is introduced. “Noise-based” and “non-parametric” imply that this technique imposes negligible constraints on the properties of the targets and that it employs no regression analysis or fittings. The sub-sky detection threshold is defined and initial detections are found, independently of the sky value. False detections are then estimated and removed using the ambient noise as a reference. This results in a purity level of 0.89 for the final detections as compared to 0.29 for SExtractor when a completeness of 1 is desired for a sample of extremely faint and diffuse mock galaxy profiles. The difference in the mean of the undetected pixels with the known background of mock images is decreased by 4.6 times depending on the diffuseness of the test profiles, quantifying the success in their detection. A non-parametric approach to defining substructure over a detected region is also introduced. NoiseChisel is our software implementation of this new technique. Contrary to the existing signal-based approach to detection, in its various implementations, signal-related parameters such as the image point spread function or known object shapes and models are irrelevant here. Such features make this technique very useful in astrophysical applications such as detection, photometry, or morphological analysis of nebulous objects buried in noise, for example, galaxies that do not generically have a known shape when imaged.

Key words: galaxies: irregular – galaxies: photometry – galaxies: structure – methods: data analysis – techniques: image processing – techniques: photometric

Free reproduction: All the data-generated numbers and figures in this paper are exactly reproducible/configurable with a make command. See `reproduce/README` in the arXiv source files. All results generated by free software.

1. INTRODUCTION

Galaxies are one of the most prominent forms of nebulous or amorphous objects in astrophysics and astronomical image processing. They appear to have a very diverse kinematic history and thus display a very large variety of shapes and forms. They also have complex three-dimensional structures which we can observe in two dimensions. Galaxy images can host an arbitrary number of clumps positioned anywhere over their light profiles. These clumps might be minor or major mergers, supernovae, other galaxies, or stars on the same line of sight, or highly localized unobscured star-forming regions. With such hurdles, astronomical image processing, and in particular galaxy morphological analysis, can be considered one of the most demanding of all disciplines in image processing.

Observations are inevitably diluted with noise. Any systematic bias in measuring the noise properties will directly propagate to all higher level measurements on the detected signal or scientific targets. Therefore, accurately measuring the noise characteristics is the most fundamental and primary issue in data analysis and subsequent astrophysical interpretations. However, noise can only be accurately characterized when the signal or object(s) buried in the noise are detected and removed. Therefore any difficulties in detection can directly translate into a systematic bias in the measured noise properties. For example, objects that are very faint and diffuse overall are very hard to detect. For brighter objects that can be detected, identifying the possible boundaries is a major concern. The uniformity in shape, or morphology, between various objects can also play a significant role in the detection ability.

Detection of nebulous astronomical targets significantly suffers from all the problems mentioned above. Because of the in-

strument and atmospheric point spread function (PSF) and also the intrinsic shapes of galaxies, their profiles sink deep into the noise very slowly with a hardly detectable clear cutoff. Astronomical targets also have an extremely wide range of apparent luminosity and surface brightness profiles, from very bright nearby stars and galaxies to faint objects far below the detection limits.

The most commonly used detection methods in astronomy, regardless of their implementation, can be classified as *signal-based* detection (see Appendix B for a review). The signal’s a priori known properties are the basis of this method. Thus the inherent shape (for example, being an ellipse or a functional radial profile) of the galaxies and the atmospheric and instrumental effects, or PSF, have to be known prior to running the detection algorithm. This approach to detection will therefore be most accurate for objects that satisfy the a priori known shapes and will become less reliable as the inherent shapes of the targets deviate from the expected shape. Failing to correctly find the PSF will also hamper the accuracy of the results.

Systematic biases that are caused by cosmological surface brightness dimming along with K corrections and morphological evolution can hamper the accuracy of any study attempting to compare galaxy populations at different redshifts. Therefore it is very important that the detection and measurement tools used can provide less biased results. An example of such comparisons is the observed morphological evolution of blue galaxies where it has been observed that at higher redshifts ($z > 1$), a larger fraction of galaxies display irregular or clumpy morphologies compared to their lower- z counterparts (Cowie et al. 1995; Abraham et al. 1996; Lotz et al. 2006; Elmegreen et al. 2007; Murata et al. 2014). This observed morphological evolution biases the photometric measurements of any detection method that

is based on a fixed elliptical shape and surface brightness profile for all redshifts, for example, the Petrosian (1976) and Kron (1980) methods. It is currently thought that the the peak of cosmic star formation density was at $z \sim 2$ (Hopkins and Beacom 2006; Kajisawa et al. 2010; Lundgren et al. 2014). Hence, the spatial variation of star formation activity within these earlier galaxies or their star formation morphology is instrumental in understanding star formation in the galaxies.

The concordance or Λ CDM cosmological model is another field that heavily depends on detection ability. It predicts much fainter, lower surface brightness dwarf galaxies than currently observed and may be lurking below the currently used detection thresholds (Kauffmann et al. 1993; Klypin et al. 1999). From the theoretical point of view, changing the astrophysical constraints of the semi-analytic models results in the simulations and observations becoming more consistent (see Macciò et al. 2010, and references therein). However, an observational confirmation is still lacking. Since such low mass galaxies are very faint and have irregular/amorphous morphologies, existing detection methods that rely on an ellipse and a priori known radial profiles are insufficient and new detection methods that do not have this limitation might provide the solution from the observational point of view.

In the study of individual galaxies, the faint outer wings are a treasure trove for expanding our knowledge of galaxy evolution. Being much less affected by internal processes, the fainter outskirts of galaxies preserve valuable information about the dynamic history of the galaxy. For example, finding tidal tails present in these regions can be a very good indicator of possible previous merger events (for example, see Ellison et al. 2013). Accurate detection of the galaxy light profiles at large radii is also very dependent on the detection technique and Sky subtraction (see Section 2.2). It has been observed that the radial profiles of star-forming galaxies deviate from a purely exponential profile at large radii (for example, see de Grijs et al. 2001; Pohlen and Trujillo 2006). Successfully detecting this behavior in the outskirts can help explain the dependency of the star formation on gas surface density (Kennicutt 1989; Kregel and van der Kruit 2004).

Intra-cluster light is another field in galaxy evolution that relies heavily on the ability to accurately detect and subtract the faintest parts of cluster galaxies. These regions harbor stars that have been stripped from the galaxies but are gravitationally bound to the cluster (see Presotto et al. 2014, and references there in). Using creative and simple hardware (Abraham and van Dokkum 2014), van Dokkum et al. (2015) recently found 47 very low surface brightness but large galaxies in the comma cluster. Some of them could be visually confirmed in archived images but remained undetectable using the existing detection methods due to their very diffuse structure.

Increasing the detection ability by using larger and more accurate hardware is one the primary reasons that new telescopes and cameras are being commissioned. Over the past several decades the instruments used for astronomical observations have undergone significant advancements from analog photographic plates to digital CCDs. However, the most commonly used detection techniques still rely on the Petrosian (1976) or Kron (1980) approximations or de Vaucouleurs (1959) or Sérsic (1963) profile fittings. These functions are defined on a continuous space, so they can be considered analog techniques. The detection technique introduced in this paper exploits the digital nature of mod-

ern data sets. Most of the operation is done on the noise (undetected regions), which is also used as the basis for identifying false detection and segmentation results. Therefore statistically significant prior knowledge of signal-related properties becomes irrelevant. It also makes no use of any regression analysis or fitting which will bias the results when the targets deviate from the required model functional forms.

In Section 2 the properties of the images used and some definitions are provided. The new noise based solution is fully elaborated with images showing every step in Section 3. In Section 4 application of the concepts on a large image for increased accuracy and efficiency is explained. In Section 5 the success in detection and the purity of the proposed algorithm on mock images with mock noise is analyzed. Results on mock profile and noise are only used for this “proof of concept” paper, a full completeness, purity, number count, and etc, analysis on real images with no mock profiles will be provided in a companion paper (M. Akhlaghi et al. 2015. in preparation). Finally, in Section 6 the usefulness of this approach for existing and future astronomical research is discussed. In Appendices A and B the existing approaches to calculating the Sky and detection and segmentation/deblending are critically reviewed. Appendix C explains a new algorithm for finding the mode of a distribution. This algorithm lies at the heart of our novel sub-Sky thresholding which is independent of the Sky value. Appendices D and E show the parameter lists used for running SExtractor and NoiseChisel.

NoiseChisel is our software implementation of the proposed technique in this paper. Throughout this paper, NoiseChisel is used to refer to the proposed new approach for detection and segmentation. NoiseChisel is distributed as part of the GNU Astronomy Utilities¹ which is a new collection of tools for astronomical data analysis and manipulation. It is being introduced here as the first astronomical software package that fully conforms to the GNU coding standards² and has been evaluated and endorsed by GNU. The copyright was also assigned to the Free Software Foundation to guarantee its “freedom” and facilitate its use and future development by the worldwide astronomical community similar to all their major “free” software projects. It integrates nicely with the GNU/Linux operating system. It can also be natively compiled and installed on most other major operating systems. The existing tools in GNU Astronomy Utilities were used for all the data analysis and displaying steps in this paper (making mock profiles, convolving, adding simulated noise, producing a catalog, cropping parts of large survey tiles, FITS image conversion to document-friendly image formats, creating masks, and calculating image statistics). The GNU Astronomy Utilities is “free” software, as defined in the GNU general public license (GPL),³ version 3.

2. DEFINITIONS

Prior to a complete explanation of the proposed new algorithm, some basic issues need to be addressed first. This new technique is non-parametric (with no functional profiles or regression-based fittings); therefore, demonstrating the concepts and steps

¹ <https://www.gnu.org/software/gnuastro/>

² The GNU coding standards define specific generally accepted requirements for software configuration, compilation, and installation as well as coding style, command line user interface, and a manual in various web-based, print, and command line formats.

³ <https://www.gnu.org/licenses/gpl.txt>

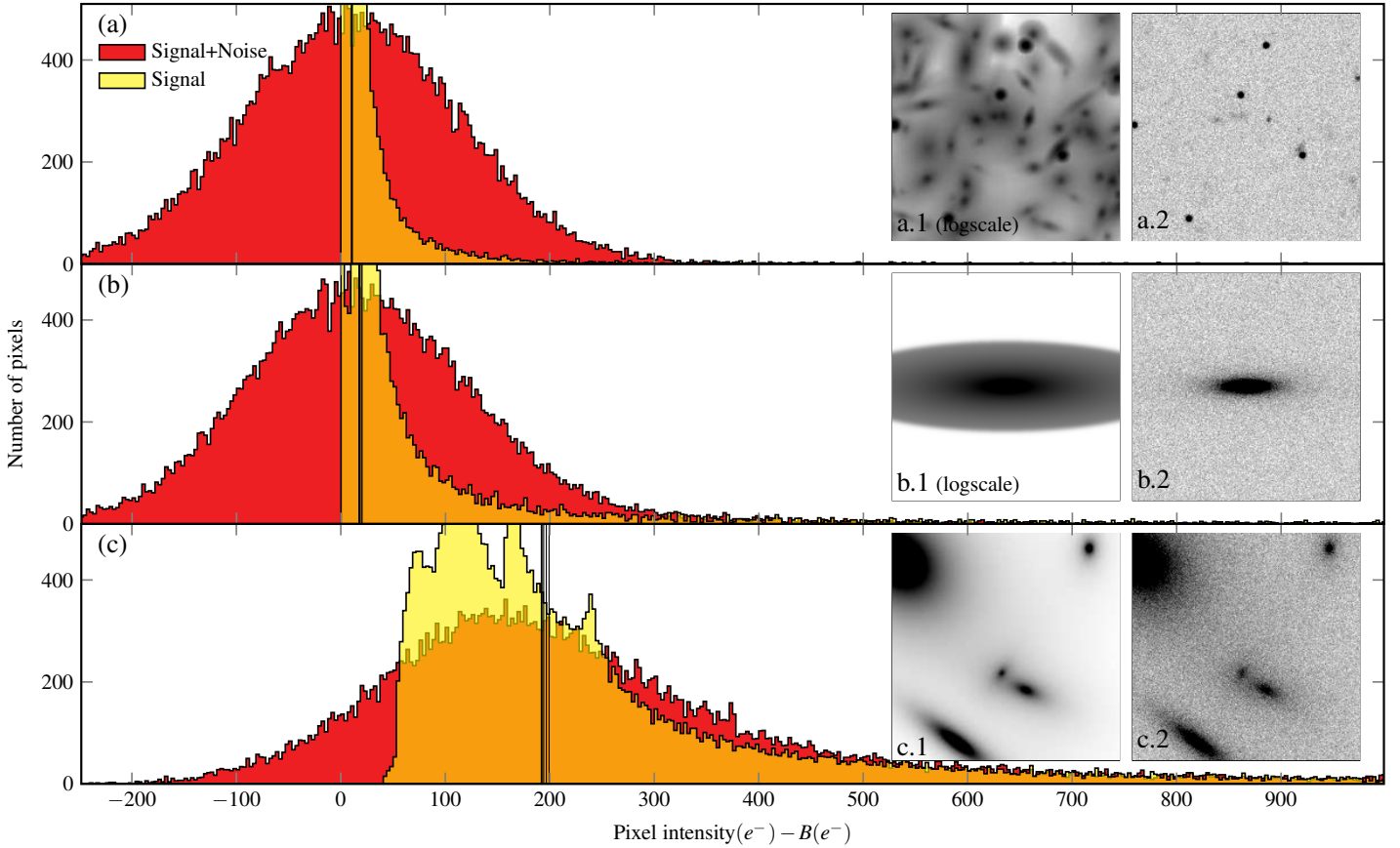


Figure 1: Mock galaxies and their pixel distributions with and without noise. The plots have two inset images. The left insets show the image of mock galaxies after convolution with a PSF prior to adding noise. Logarithmic scaling has been used for (a.1) and (b.1) to show the full extent of the light profiles. The other insets all use a linear scale. The right insets show the image of the mock galaxies with noise added. The histogram starting from or after zero (yellow) shows the pixel count distribution of the non-noised mock image (left inset). The histogram is vertically truncated for a clear comparison with the noised histogram. The wider histogram (red) shows the histogram of the noised image (right inset). The five vertical lines on each histogram show the median of the noised image after (4,5) σ -clipping (see Section A.3). Insets have been truncated to be in the range of the plot’s horizontal axis: white is -250 counts and black is 1000 counts. (a) 95 random Sérsic profiles with total magnitudes between -11 to -6 and five point sources (stars) of -12 magnitude. The zero-point magnitude for all images in this paper is set to 0.00 . (b) A -16 magnitude Sérsic profile with $n = 4.00$, $r_e = 30$ pixels, and $q = 0.25$, (c) 6 large and bright Sérsic profiles with -15 to -18 magnitude. The PSF is a circular 2D Moffat profile with $\text{FWHM} = 3$ pixels and $\beta = 4.76$ prior to adding noise. All the galaxies and the PSF are truncated at 5 times the effective radius and FWHM respectively. B is the background count, see Section 2.2.

on actual images plays a vital role in explaining the technique (Anscombe 1973). In Section 2.1 a short explanation of the postage stamps used in this paper (including the appendices) is given. Fundamentally, this new technique grew out of the definition of the Sky value, which is a very important concept in any measurement significantly affected by noise and is elaborated in Section 2.2.

2.1. Displayed Images

All the images in the figures are inverted: the darker the pixel, the larger its value. Unless otherwise stated, the displayed images are 200×200 pixels. They are all crops from original 1000×1000 pixel images. For mock images, the remaining area is filled with pure Gaussian noise and for real images, it is from the actual survey. When referring to an image by histogram, the histogram of the number of pixels at a given count level across an image or section of an image is implied, similar to those of Figure 1. The histograms only use the pixels in the displayed region, not the larger image. The vertical axis values are not displayed in all histograms beyond Figure 1, because their absolute values are irrelevant.

Unless stated otherwise, the large images were used as in-

put for SExtractor and NoiseChisel. The reason for setting these sizes was SExtractor’s modeling deficiencies in background interpolation and profile modeling on the corners and sides of the images (see Appendices A.6 and B.4). Using larger images ensures that for both programs there is an abundant area of background pixels regardless of the central object shape and size. In the purity analysis of Section 5.2 the pure noise regions of the mock images are used to identify false detections. Unless otherwise stated, all the 200×200 pixel cutouts are from the center of the larger image.

The real images used in this paper for real demonstrations are either cutouts from the COSMOS survey (Scoville et al. 2007), *Hubble Space Telescope* (HST) F814W images (see Koekemoer et al. 2007; Massey et al. 2010), or one full CCD image taken by Subaru Telescope’s SuprimeCam (Miyazaki et al. 2002).

2.2. Background, Sky, and Noise

Throughout this paper, pixel units are assumed to be in photon-counts or simply ‘count’ (e^-). All the methods can be readily applied to count sec^{-1} units. For example, all the displayed HST images were in units of counts sec^{-1} . Let us assume that all instrument defects—bias, dark and flat—have been corrected and

the total count of a detected object, O , is desired. The sources of e^- in a pixel (i, j) of the image can be written as follows: (1) contribution from the target object, O_{ij} , (2) contribution from other detected objects, D_{ij} . (3) undetected objects or the fainter undetected regions of bright objects, U_{ij} , (4) cosmic rays, C_{ij} , and (5) the background count, which is defined to be the count if none of the others exists on that pixel, B_{ij} . The total count in the pixel, T_{ij} , can thus be written as:

$$T_{ij} = B_{ij} + D_{ij} + U_{ij} + C_{ij} + O_{ij}.$$

Figure 1 shows the pixel count distribution before and after adding noise in three sample mock images. By definition, D_{ij} is detected and it can be assumed that it is correctly subtracted, so that D_{ij} can be set to zero. There are also methods to detect and remove cosmic rays (for example, the method of van Dokkum 2001), enabling us to set $C_{ij} = 0$. Note that in practice, D_{ij} and U_{ij} are correlated because both directly depend on the detection algorithm and its input parameters. Also note that no detection or cosmic ray removal algorithm is perfect. With these limitations in mind, the observed Sky value for this pixel (S_{ij}) can be defined as

$$S_{ij} = B_{ij} + U_{ij}. \quad (1)$$

Therefore, as the detection process (algorithm and input parameters) becomes more accurate, or $U_{ij} \rightarrow 0$, the Sky value will tend toward the background value or $S_{ij} \rightarrow B_{ij}$. Thus, while B_{ij} is an inherent property of the data (pixel in an image), S_{ij} depends on the detection process. Over a group of pixels, for example, in an image or part of an image, this equation translates to the average of undetected pixels. With this definition of Sky, the object count in the data can be calculated with

$$T_{ij} = S_{ij} + O_{ij} \Rightarrow O_{ij} = T_{ij} - S_{ij}. \quad (2)$$

Hence, the more accurately S_{ij} is measured, the more accurately the count of the target object can be calculated. Similarly, any under- (over-)estimation in the Sky will directly translate into an over- (under-)estimation of the measured object's count. In the fainter outskirts of an object a very small fraction of the photo electrons in the pixels actually belong to objects. In Figure 1(b.1) for example, only 19.83% of the pixels belonging to the central object have a value larger than 10100 counts while the background is 10000 ± 100 counts. Therefore even a small overestimation of the Sky value will result in the loss of a very large portion of this mock galaxy.

Based on the definition above, the Sky value is only correctly found when all the detected objects (D_{ij} and C_{ij}) have been removed from the data. However, as shown in Section B.1, existing methods define their detection threshold using the Sky value (see Section B.1.2 in particular). Therefore they cannot use this definition in finding the Sky. They have to apply the methods explained in Appendix A to approximate it. The foundation of the technique presented here is that the detection threshold and initial detection process is defined independent of the Sky value see Figure 2 and Section 3.

In the mock images in this paper each pixel value (T_{ij}) is composed of the object contribution, O_{ij} , and the background B : $T_{ij} = B + O_{ij}$; see Figure 1. The noise is added to each pixel by replacing its value with a random value taken from a Gaussian distribution with a mean of T_{ij} and $\sigma_{ij} = \sqrt{T_{ij}}$. In this

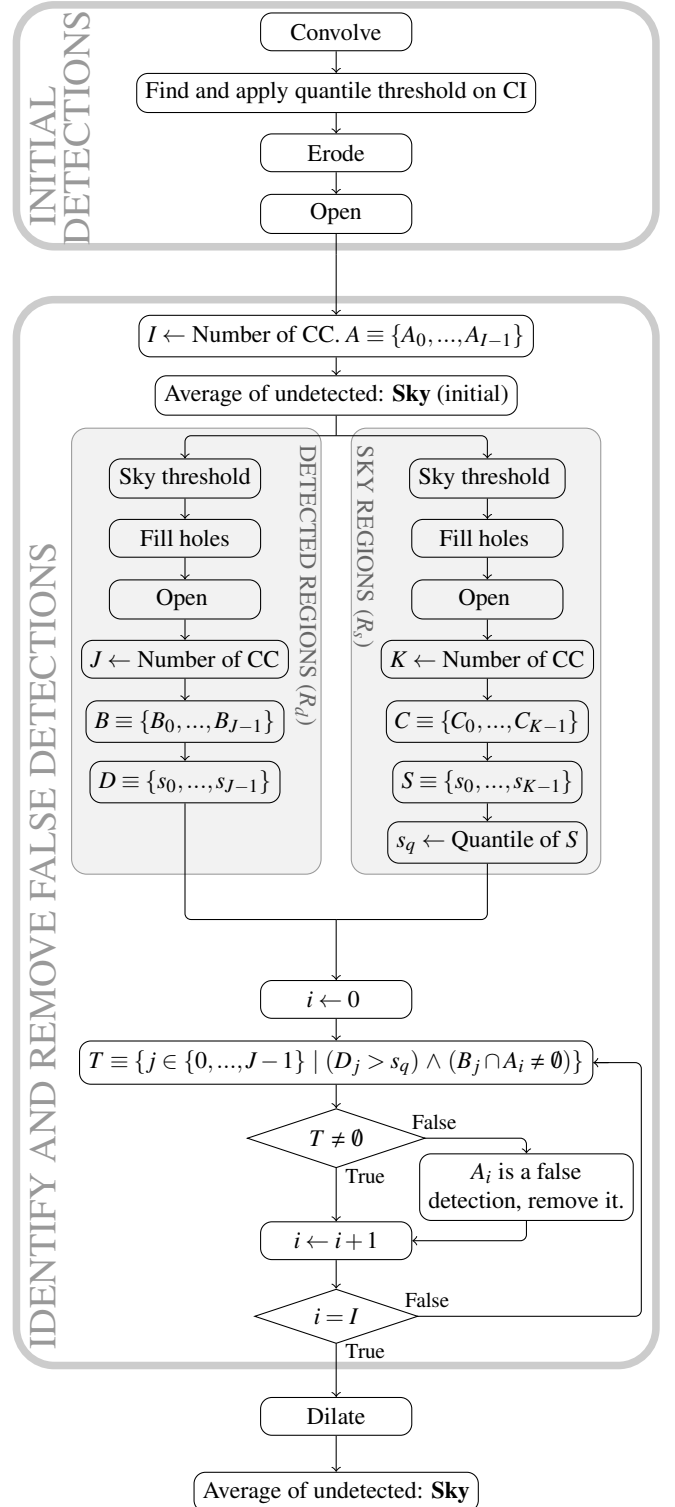


Figure 2: Flowchart of the complete detection algorithm. The steps of the top and bottom boxes can be seen in the example images of figures 3 and 7 respectively. CI stands for convolved image, CC for connected components, s for signal-to-noise ratio, \wedge for logical 'and', \leftarrow for assignment, $=$ for comparison, and \emptyset for the empty set. Each CC is defined as a set of image pixels. I is the number of CCs in column 1 of Figure 7. J and K represent the number of CCs in the bottom and top of column 4 in Figure 7, respectively. A_i , B_i , and C_i are sets of pixels belonging to the i th connected component in their respective images. A , B , and C are families of sets (connected components). D_i and S_i are the total signal-to-noise ratios of B_i , and C_i respectively.

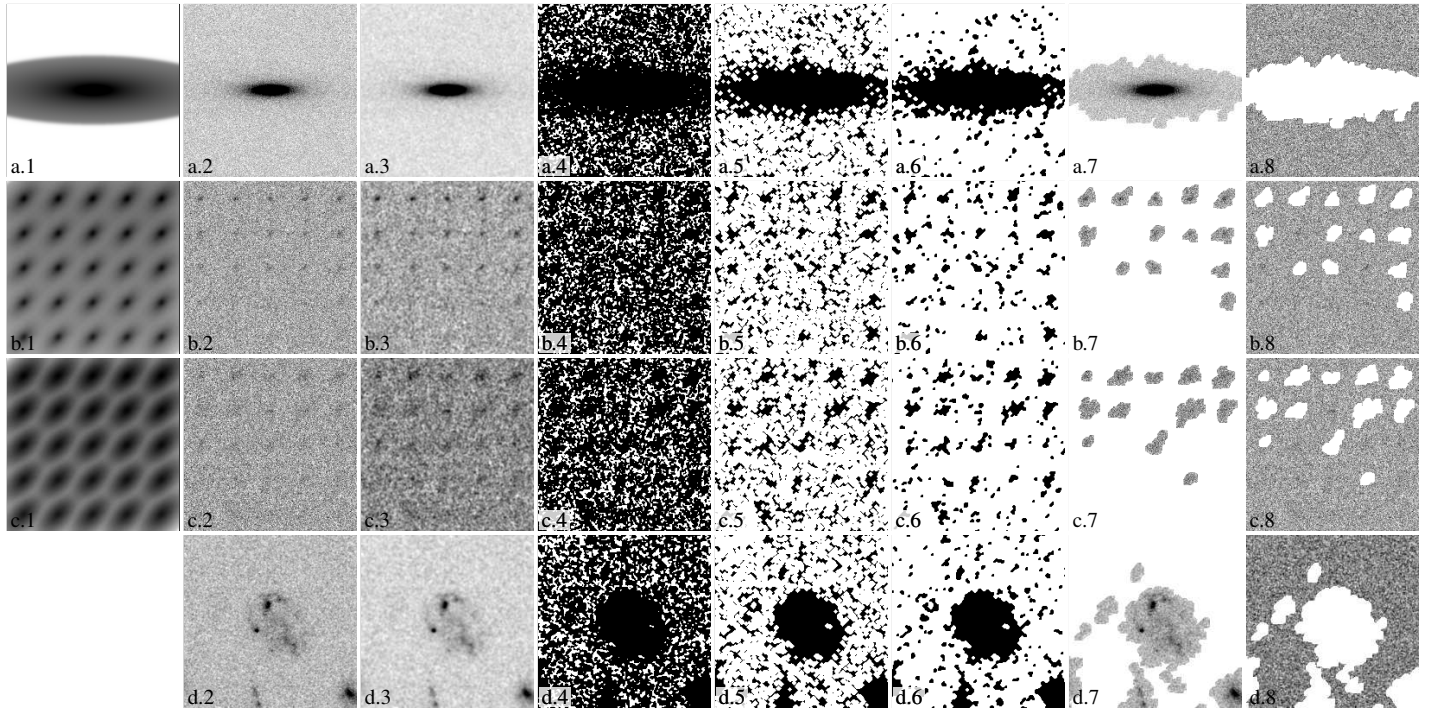


Figure 3: Demonstration of major detection steps in NoiseChisel. The rows are (a) the same mock profile as in Figure 1(b). (b) 25 mock profiles with the same parameters with $n = 4$ (see Section 3.1), (c) similar to (b), but with $n = 1$, (d) a real star-forming $z \sim 1.5$ galaxy imaged in *HST*/ACS F814W. The columns represent (1) mock profiles before the addition of noise and blank for the real image (it is blank since the signal without noise is not known in a real image; All mock images in this column are plotted in the logarithmic scale), (2) noisy image, (3) convolved with a 2D Gaussian kernel of FWHM = 2 pixels, (4) threshold applied on the 0.3 quantile of the convolved image, (5) 4 connected erosions applied 2 times, (6) 8 connected opening applied 1 time, (7) estimated false detections removed (see Figure 7; true detections are dilated two times and undetected pixels masked; pixel values are taken from the noisy image in column 2), and (8) the inverse of column 7. Columns 3 – 6 (inclusive) correspond to the top four steps of the flowchart in Figure 2.

paper, $B = 10000e^-$. The magnitude of each object is defined as $-2.5 \log(F)$, where F (sum of pixel values) is in e^- . In other words, the zeropoint magnitude is 0.00 since this paper is not limited to any particular instrument. So the background magnitude is -10.00 . The total magnitude is calculated from the sum of all the object pixels in the image (not integrated to infinity). All profiles are truncated at $5r_e$.

3. NOISECHISEL

The general flowchart of the proposed technique can be seen in Figure 2. In the proposed algorithm, a Sky-independent approach is used to arrive at an *initial* detection. Individual initial detections are subsequently classified as true or false based on their signal-to-noise ratio (S/N) using the surrounding undetected regions as a basis. As seen in Figure 2, this second classification step requires an initial measurement of the Sky value as the average of the initially undetected pixels and is fully elaborated in Section 3.1. The substructure in each detection is then found and classified through defining “clumps” and “objects” which is explained in detail in Section 3.2.

The input parameters⁴ for NoiseChisel are specified in the text with `--parametername=value`.⁵ The values used for the parameters of NoiseChisel reported here are chosen such that once applied to the mock and real image tests that are shown

⁴ Not to be confused with the non-parametric basis of this algorithm. By non-parametric it is implied that there are no functions and fittings, not that there are no parameters.

⁵ This is similar to the long format of how the options should be called on the command line in NoiseChisel.

in this paper, accurate results are achieved. The full parameter list can be seen in Appendix E. The criteria are to have fewer false detections in pure noise while detecting the faintest pixels of the mock profiles (see Section 5). We do not claim that these are “the best” set of parameters for any generic data set.

3.1. Detection and Sky

The basic idea behind this detection algorithm is that if there is a true signal buried in the noise over a certain *contiguous* area, it will systematically (contiguously) augment that region (keeping the noise fluctuations). The steps explained here are specifically designed to best separate these connected, augmented regions deep in the noise. The initial detection steps in NoiseChisel are schematically shown in the top group of steps of the flowchart in Figure 2 and their application to sample images is demonstrated in Figure 3. First, a very small FWHM kernel is convolved with the image (Section 3.1.1, column 3 in Figure 3). A very low threshold is then applied to the smoothed image (Section 3.1.2, column 4). The regions below the threshold are expanded by eroding those that are above it (Section 3.1.3, column 6). Since the objects are not completely separated yet, “opening” is applied (Section 3.1.4, column 7). False detections are estimated and removed (Section 3.1.5) and the fainter regions of true detections, which were carved off during erosion are returned in a process of dilation (Section 3.1.6).

Three of the examples in Figure 3 are mock and one is a real galaxy. Figure 3(a) is the same mock profile as in Figure 1(b). Figures 3(b) and (c) contain 25 mock 2D Sérsic profiles placed with equal spacing on a grid across the image. Other

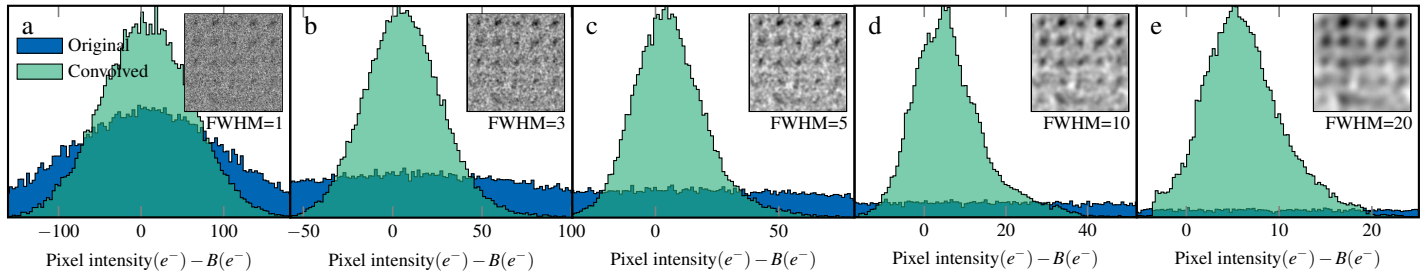


Figure 4: Effect of convolution with wider kernels on Figure 3(c.2). The green histogram shows the count distribution of the convolved image. The blue histogram shows the distribution of the original image pixel count values within the green histogram’s range. The convolution kernel used is a Moffat function with $\beta = 4.76$ (same as the PSF used for the mock images), while the FWHM is shown for each in units of pixels. Each kernel is a square of side $5 \times \text{FWHM}$ pixels. Note how the convolved histogram becomes more skewed as a wider kernel is used for convolution. The range of the horizontal axis significantly decreases with increasing kernel width. B is the background count, see Section 2.2.

than their magnitude and position, all of the parameters are equal with a position angle of 45° , an axis ratio of $q = 0.5$, and an effective radius $r_e = 10$ pixels. The Sérsic index (n) of all the galaxies in each image is also the same. The bottom left profile is the faintest with -9.2 magnitude. The next profiles are successively -0.06 magnitudes brighter towards the top right. Such extremely faint profiles were intentionally chosen to push NoiseChisel (and SExtractor in Section B.1.3) to the limits. Figure 3(d) shows the same steps with exactly the same parameters applied to a real $z \sim 1.5$ star-forming galaxy in the COSMOS field imaged with the *HST* Advanced Camera for Surveys (ACS) using the F814W filter.

3.1.1. Convolution

Convolution is used to maximize the ratio of an object’s peak signal to the local noise level (Bijaoui and Dantel 1970; Irwin 1985). Convolution smooths the image by removing high spatial frequencies. This means that after convolution, “nearby” pixels with large differences in value, which are commonly due to noise, will receive an intermediate value. Therefore, by smoothing the noise, the fraction of signal-to-noise is increased. Without convolution, the large spatial frequencies due to noise will significantly limit the ability to detect a contiguous region in noise. Hence, in order to maximize the detection ability, convolution is necessary. The definition of a *nearby* pixel and the functional form of how to define the intermediate value are defined with the kernel input into convolution.

Figure 4 shows the noised image of 25 very faint $n = 1$ profiles, convolved with increasingly wider (larger FWHM) kernels applied. As the kernel used for convolution widens, the image becomes more and more blurred, its histogram becomes more skewed, and the range of pixel values (dynamic range) in the image decreases with more pixels having similar values. Comparing the blue and green histograms in Figure 4 shows this effect. The skewness induced into the histogram is another manifestation of the increase in the S/N of connected objects. Due to the skewness, separation of the brightest sections of the objects from the noise is facilitated. A wider convolution kernel has important consequences. (1) The shapes of the object tend to the shape of the kernel used to convolve the image. (2) The dynamic range significantly decreases. Therefore, separating the fainter parts of the brighter objects from noise becomes much harder. (3) Compact and faint objects, that is, those that are not wide relative to the convolution kernel, will be lost.

The effects above are particularly harmful in ground-based

images, where the FWHM is generally very large. The decrease in the dynamic range is not a considerable issue in the signal-based technique because only the brightest pixels of the objects are sought and the fainter parts are modeled (see Section B.4). As seen in the sequence of steps in Figure 3, the proposed detection technique is exactly the opposite and aims to impose negligible constraints and models on the detected signal. The dynamic range is hence extremely important to successfully find the faint but valuable object pixels. Therefore a sharp convolution kernel is used.

Unlike contiguous (multi-pixel) signal, noise is ideally independent from pixel to pixel,⁶ and thus is directly connected with sampling or pixel size. Inverting the Nyquist sampling theorem, the sharpest convolution kernel can be considered an FWHM= 2 pixel kernel and a Gaussian is used for its functional form. In all the examples in this paper, mock or real, ground-based or space-based, a Gaussian profile with FWHM= 2 pixels truncated at five times the FWHM is used, so that the kernel is 11×11 pixels⁷. The fact that the same convolution kernel gives very accurate results on any type of image is one example of the objectivity of NoiseChisel’s output.

Throughout NoiseChisel, the convolved image is only used for relative pixel values, for example in thresholding (Section 3.1.2) or oversegmentation (Section 3.2.1). The input image is used for absolute pixel values, for example, the Sky value, the magnitude of an object, or its S/N. This distinction is not commonly practiced in most existing techniques. For example, in SExtractor, the threshold value is found from the input image and applied to the convolved image; see Section B.1.2.

3.1.2. Thresholding

Pixels with values far below the inherent background or measured Sky values (see Section 2.2) can harbor valuable information (see Figure 1). After accurate Sky subtraction, a real object will always have a positive total count. However, the standard deviation of the noise is always much larger than the smallest detectable positive count value of the real objects. For example, assume that the Gaussian noise standard deviation is $30e^-$. After accurate Sky subtraction, $\sim 37\%$ of⁸ the pixels that harbor $10e^-$

⁶ In processed images we have correlated noise which is addressed in Section 3.1.5.

⁷ The convolution kernel is created with MakeProfiles which is part of the GNU Astronomy Utilities. The non-zero pixels in the square kernel have a circular shape.

⁸ The cumulative distribution function of a normal distribution with mean of $10e^-$ and standard deviation of $30e^-$ calculated at $0e^-$.

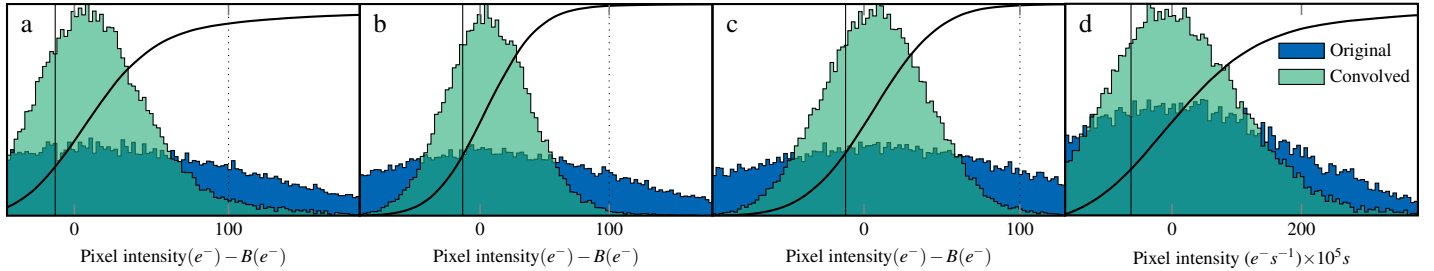


Figure 5: Thresholds used in the demonstration examples of Figure 3 with the same labels. The blue histograms belong to the actual image (column 2 in Figure 3). Only the range that overlaps with the green histogram is plotted here. The green histogram is the histogram of the convolved image (column 3 of Figure 3). The thick curve shows the cumulative frequency of the convolved image. The thin solid vertical lines show the 0.3 quantile of the convolved image which is used to determine the threshold for it; this value is used to make column 4 of Figure 3. The dotted lines in the first three examples (mock galaxies) show the ideal σ_{sky} of the input image (blue histogram), which is $100e^-$. B is the background count, see Section 2.2.

of real counts will have negative recorded pixel value. Once a large number of such pixels are found and the Sky value is accurately subtracted, the random effects of noise will be decreased and useful information can be extracted from such pixels.

Therefore it is wrong to assume that the Sky value is the lowest possible threshold. To accurately detect the faintest pixels of an object, the threshold has to be less than the Sky value. This is very important in accurate measurement of the Sky value as the average of undetected pixels.

In NoiseChisel the threshold is defined using the cumulative distribution of the pixels in the convolved image. To ensure that the threshold is below the Sky value, the quantile has to be less than 0.5, or the median. For the examples in this paper, the quantile threshold is set to `--qthresh=0.3`, which means that 70% of the pixels in the convolved image will have a value above it. The results of applying a threshold to the convolved image can be seen in Figure 3, column 4, where black pixels are the ones that had a count above this threshold. The thresholds can be seen relative to the actual and convolved image histograms in Figure 5. Notice that the threshold is safely below the background value which is $0e^-$ for the mock images. In Section 4.2.1 the complete procedure for finding the threshold on a large image is elaborated.

3.1.3. Erosion

Applying a threshold to the image (Section 3.1.2) results in a binary image with pixels either having a count above the threshold or below it. The former are known as foreground pixels which are black in Figure 3, column 4. The latter, called background pixels, are displayed in white in the same figure. Because of this extremely low threshold, it is clear from column 4 of Figure 3 that the regions harboring true signal in them cover a 2D contiguous (non-porous) region of connected pixels, while regions where no data is present form a porous structure in the foreground. The figure shows that when signal is present, even if it is very close to the background value, it will augment the region that it covers. The augmentation can be seen through smaller and fewer white holes in the black regions that harbor data. The first step in NoiseChisel after applying the threshold is thus to exploit this porous structure and expand the holes through erosion of the foreground to separate the augmented regions.

Erosion is an operation in morphological image processing (Starck and Murtagh 2006; Gonzalez and Woods 2008). By eroding the foreground, it is implied that all foreground pixels

that *neighbor* a background pixel are carved off⁹ the foreground and changed to a background pixel. The neighborhood of, or connected pixels to, a pixel is defined based on a *structuring element* and generally has two types: 4 and 8 connectivity (see Figures 6(a) and (b)). Eroding based on 8 connectivity will remove more pixels. Therefore, in this step, NoiseChisel uses a 4 connected structuring element to erode the foreground. The statistical properties of this and other operations in mathematical morphology are reviewed in Dougherty (1992).

Eroding the foreground expands the holes (white regions in Figure 3 column 4) and connects them to each other. The best number of erosions (`--erode`) and the type of connectivity (`--erodengb`) applied to an image is intertwined with `--qthresh`. The results of respectively setting them to 2 and 4 can be seen in Figure 3, column 5. If a set of foreground pixels had the shape of the non-white pixels of Figure 6(c), after applying this erosion the pixels with the two brighter shades of gray would be carved off and only the central 9 pixels would remain.

3.1.4. Opening

Dilation is the inverse of erosion in morphological image processing. When dilating the foreground, if a background pixel touches a foreground pixel, it will be changed to the foreground. Applying these two steps in order, namely, first eroding then dilating the foreground, is known as *opening*.

Opening is very useful for separating regions of the foreground that are only connected through a thin thread of pixels. It also has the benefit of removing extremely small objects (see Vollmer et al. 2013, for such an application in astronomy). If the image is first eroded n times and then dilated the same n times, then n is referred to as the “depth” of the opening. Note that the erosion discussed here is part of opening and separate from the one in Section 3.1.3. The depth can be set in NoiseChisel through the parameter `--opening` and the type of connectivity can be set through `--openingngb`. In the examples shown in Figure 3, they are set to 1 and 8, respectively. The opened image can be seen in column 6 of Figure 3. Compared with column 5, it is clear that, as expected, opening has separated the foreground into separately connected regions or islands without bridges.

Multiple erosions and dilations with the same structuring element will result in the outer shapes of the foreground becoming like a diamond in 4 connectivity or a rectangle in 8 connectivity. Therefore, since the erosion of Section 3.1.3 was based on

⁹ Hence the name NoiseChisel: a tool for carving off noise, similar to what wood chisels or stone chisels do on their respective materials.

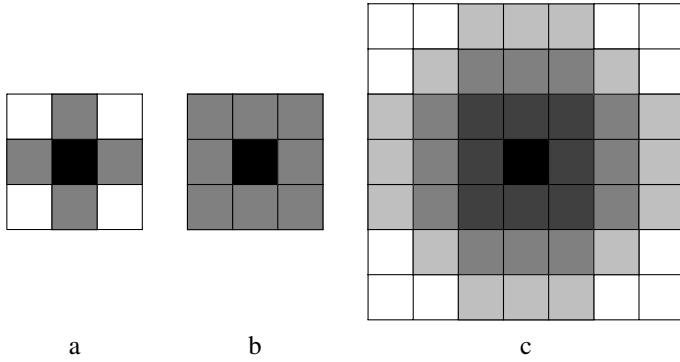


Figure 6: Structuring elements. The black pixel is the pixel under consideration and the gray pixels are the neighbors of that pixel. (a) 4 connected neighbors. (b) 8 connected neighbors. (c) Non-white pixels show the smallest area an object should have to be detected with the given two 4 connected erosions (see Section 3.1.3) and one 8 connected opening (see Section 3.1.4). It is assumed that all the pixels outside the box shown are background (white). The three shades of gray show the pixels that are removed in each step (brightest first). After the three steps finish, the inner 9 pixels remain. In processing, white pixels have a value of 0 and others have a value of 1.

a 4 connected structuring element, in this step an 8 connected structuring element was used to compensate for the shape loss in the previous step as well as more successfully removing thin connections. The composite effect of the two steps of erosion in Section 3.1.3 and the opening done here can be seen in Figure 6(c). Before the dilating section of the opening step, only the central black pixel will remain. If a region above the threshold is any smaller than the colored pixels of Figure 6(c), it will disappear after this step since no pixels remain for dilation.

The erosion and dilation defined here are based on a binary image as discussed in Section 3.1.3. It is also possible to define such operations on grayscale images where a pixel can have a range of values, not just 0 or 1. Perret et al. (2009) used a combination of such grayscale erosion and dilation (hit-or-miss transform) for a demonstration on detecting low surface brightness galaxies. Since the structuring element is no longer a binary, the variation of pixel values over the structuring element becomes very important and has to be modeled based on specific elliptical parameters, surface brightness profiles, and the PSF; see Figures 4 and 5 of Perret et al. (2009). Therefore, it is optimal only for profiles that satisfy the count distribution of the structuring element. Applying it generically to any image with any distribution of galaxy morphologies will require a high level of customization that may fail for complex galaxy morphologies like the real galaxies shown in this paper.

3.1.5. Defining and Removing False Detections

The foreground is now composed of separately connected objects that we define as *initial* detections. However, on the mock images (particularly comparing Figure 3(a.1) with (a.6)), it is clear that some detections can be associated with true signal while most cannot. These “false” detections are sets of pixels with random values (above the very low threshold on the convolved image) that were randomly positioned close enough to each other to pass the erosion and opening steps of detection explained above. As the threshold decreases, the probability of such random positioning increases. If a larger threshold, number of erosions, or number of openings is used, false detections will decrease or completely disappear.

The problem with more stringent detection parameters is that

besides rejecting more inherently faint objects, they will also remove the valuable fainter parts of the final detections. Therefore, a classification scheme is defined to find and remove false detections very accurately. This allows for keeping the valuable faint pixels of bright detections and most of the detections that would have been lost otherwise.

The bottom group of steps in the flowchart in Figure 2 show all the steps used to define and remove false detections. The same steps can also be seen in practice in Figure 7 and elaborated here. The detections have divided the pixels into 2 sets: (1) The undetected sky, R_s (white regions of column 1 in Figure 7) and (2) the detected regions, R_d (black regions in column 1 of Figure 7). It can be reasonably assumed that no significant contribution from a detectable object exists in R_s . Some of the detections in R_d harbor signal and some are localized random noise pixels, namely false detections.

In order to identify the false detections in R_d , a secondary detection process is applied to the pixels of both R_s and R_d independently. The detections in the former will provide a scale on which the certainty of the detections in the latter can be defined. Let S_a and σ_s be the average and standard deviation of the count in R_s , respectively. The second threshold is defined by these two parameters. Note that this S_a is not the final Sky value because some of the high valued, localized noise pixels (false detections) have systematically been removed from it; it is just used here as an approximation.

The user is free to set this second threshold based on $S_a + d_{\text{thresh}} \times \sigma_s$. In the examples here, $--d_{\text{thresh}} = -0.1$. The result of applying this threshold to the detected and blank regions can be seen in Figure 7, column 2. Note that as discussed in Section 3.1.1, absolute values such as S_a and σ_s come from the input image. Therefore, while the pixel *indices* comprising R_s and R_d are defined from column 6 of Figure 3, which used the convolved image, the pixel *values* for finding and applying this second absolute threshold come from the actual image. The pixels that were above this threshold are marked in black in column 2 of Figure 7.

As discussed in Section 3.1, a significant advantage of data over noise detections is that the data augment a *contiguous* region. In order to exploit this contiguous property of true detections, all the holes that are engulfed in 4 connected foreground regions will be filled. Note that holes are white pixels in Figure 7, column 2. The result of filling such holes can be seen in column 3 of Figure 7. Such holes are most probably due to noise since the 4 connectivity of all the surrounding pixels is a very strong constraint (compare Figure 7(b.2.2) and (b.3.2)). Combined with the next step (opening), filling holes in this manner significantly enhances the ability to identify a faint contiguous signal.

To remove the thin connections between thicker regions and obtain individual connected components, one level of 4 connected opening is applied. The result can be seen in column 4 of Figure 7. The two images of column 4 in Figure 7 are now composed of separate connected components (pseudo-detections) that were created in exactly the same manner but on different regions of the input image. The parameter used to quantify the definition of a false detection is the total S/N (S/N_T) of each pseudo-detection which is a combination of its total count and area.

Let F be the average count in each pseudo-detection and N be its area. The areas vary widely, ranging from one pixel to thousands of pixels. Therefore in order to get a reasonable

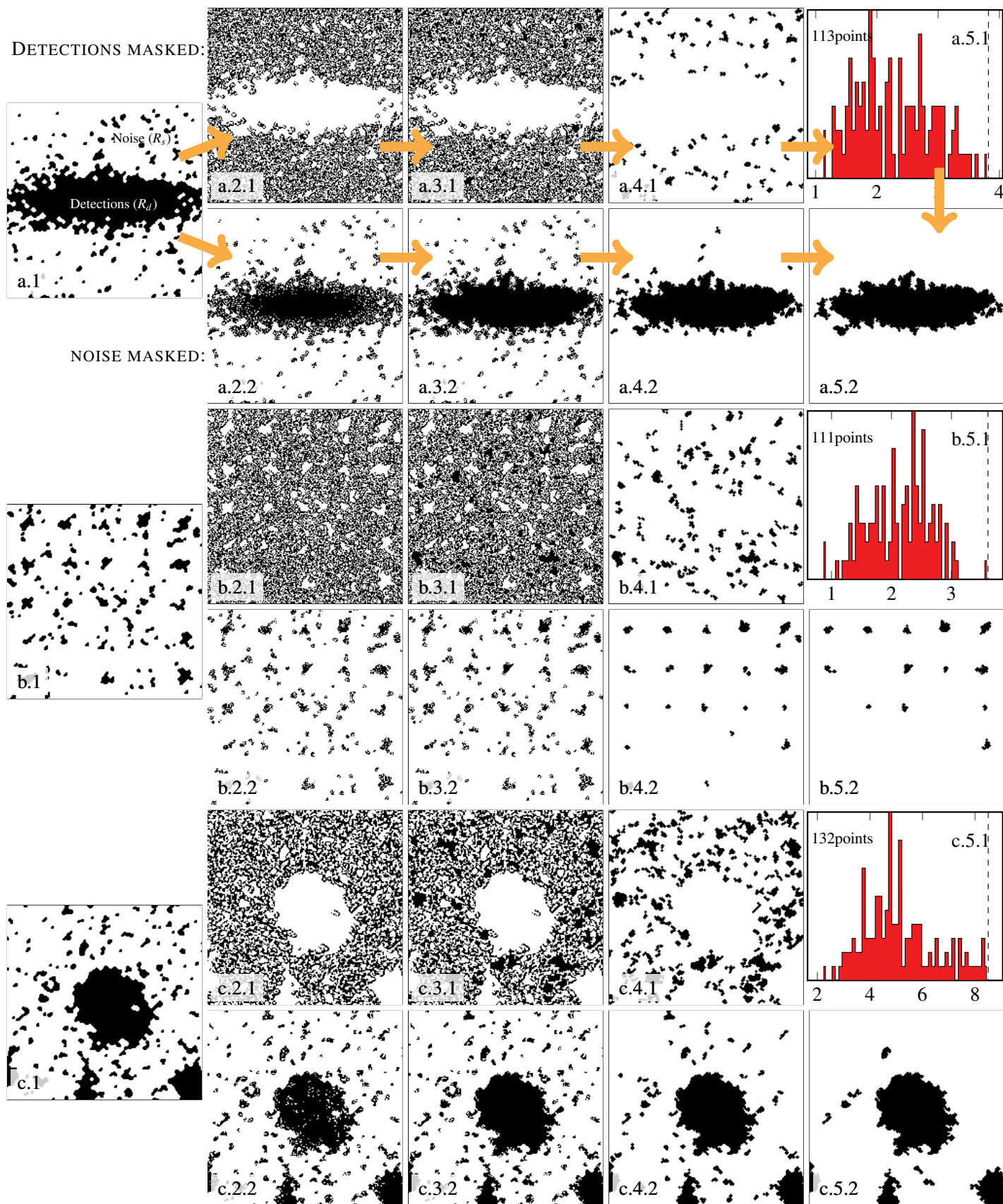


Figure 7: Identifying and removing false detections, demonstrated for three of the examples from Figures 3(a), (b) and (d). Column 1 is the same as column 6 in Figure 3. Columns 2 to 4 apply the same steps (explained below) on the undetected regions (top) and detections (bottom) separately. Column 2: Applying the threshold. Column 3: Fill holes surrounded by one 4 connected region above the threshold. Column 4: Application of opening to the previous column and small regions removed. Column 5, top: distribution of the total signal-to-noise ratio of all the dark connected components in column 4 (top). The dashed vertical line in the histogram shows the $--detquant=0.99$ quantile of this distribution. This value is used as a threshold to define false detections in column 4 (bottom). (a.5.1) is from a nearby large mesh (see Section 4) because the number of connected components in (a.4.1) is less than $--minnumfalse=100$. Column 5 (bottom): all detections with total signal-to-noise ratio above that threshold. The arrows in (a) visualize the steps which are schematically shown in the lower box of Figure 2.

average count comparison, all pseudo-detections with an area smaller than `--detminarea` are removed from the analysis in both R_s and R_d . In the examples in this section, it is set to 15. Note that since a threshold approximately equal to the Sky value is used, this is a very weak constraint. For each pseudo-detection, S/N_T can be written as,

$$S/N_T = \frac{NF - NS_a}{\sqrt{NF + N\sigma_S^2}} = \frac{\sqrt{N}(F - S_a)}{\sqrt{F + \sigma_S^2}}. \quad (3)$$

See Section 3.3 for the modifications required when the input image is not in units of counts or has already been Sky subtracted. The distribution of S/N_T from the objects in R_s for the three examples in Figure 7 can be seen in column 5 (top) of that figure. Image processing effects, mainly due to shifting, rotating, and re-sampling the images for co-adding, on the real data further increase the size and count, and hence, the S/N of false detections in real, reduced/co-added images. A comparison of scales on the S/N histograms between the mock ((a.5.1) and (b.5.1)) and real (c.5.1) examples in Figure 7 shows the effect quantitatively. In the histograms of Figure 7, the bin with the largest number of false pseudo-detections respectively has an S/N of 1.89, 2.37, and 4.77.

The S/N_T distribution of detections in R_s provides a very robust and objective scale that can be used to select or reject a given detection in R_d . The level of certainty for true detections can be input by the user and is defined based on `--detquant` which is the desired quantile in the S/N_T distribution of R_s . In the flowchart shown in Figure 2, this is displayed with $D_j > s_q$. The accepted detections from the second thresholding can be seen in the bottom row of column 5 in Figure 7. Any initial detection that overlaps with at least one of the accepted pseudo-detections ($B_j \cap A_i \neq \emptyset$ in Figure 2) is defined as a true detection, while those that don't are considered a false detection and removed. The successful detections can be seen in the last two columns of Figure 3 (after a final dilation; see Section 3.1.6).

Outside of astronomical data analysis, the technique proposed here to separate true from false detections (and later clumps; see Section 3.2.1) can be considered a form of anomaly detection in data mining. An anomaly or outlier is defined as “an observation which deviates so much from other observations as to arouse suspicion that it was generated by a different mechanism” (Hawkins 1980, page 1). This is a very general and qualitative definition applicable to any form of anomaly (see Chandola et al. 2009, for a review).

The S/N of the connected components in R_s (after applying the threshold, filling holes, and opening) gives a scale to define the outliers in R_d (true pseudo-detections). However, a quantile and not the histogram is used (the histogram is only displayed in Figure 7 for demonstration). Therefore based on the classification of Chandola et al. 2009, the true/false classification technique proposed here can be considered a non-parametric, “quantile based” statistical anomaly detection technique.

This technique for determining an “anomaly” (or a real object within noise) has some similarities to the Higher Criticism statistic (Donoho and Jin 2004). It was used in detecting non-Gaussianities in the cosmic microwave background (Cayón et al. 2005) with the modification of using p -values. However, the higher criticism statistic is derived from and applied to the same set of observations, while here the S/N threshold is found using a completely separate set of pixels (those in R_s). It is then applied

to another set of pixels (R_d). Also, while the Gaussian/Poisson distribution is assumed for the noise, there is no such assumption for the distribution of the S/N.

3.1.6. Final Dilation

The final step is to restore, through dilation, the pixel layers of each remaining initial detection that were removed by erosion in Section 3.1.3. Dilating `--erosion` times would presumably restore the object pixels out to the initial `--qthresh` quantile. The user can set the number of final dilations with the `--dilate` option. Images of astronomical objects never have a strong cutoff. Even if they have a physical cutoff, the PSF will soften any sharp boundary except cosmic rays which are independent of the PSF. Therefore it can be assumed that the object extends beyond the initial threshold. To exploit this fact, this final dilation is only based on 8 connectivity and in the examples of this paper; it is set to `--dilate=3`.

3.2. Segmentation

The detection thresholds used are extremely low in NoiseChisel (see Section 3.1.2). Combined with the fact that galaxies have no clear cutoff, it often happens that several apparently nearby objects on the image will be detected as one region. There are two approaches to separating a detected region into potentially several sub-detections or to find substructure: segmentation and deblending.

Segmentation is the procedure that assigns each pixel to one sub-component. Deblending, on the other hand, identifies the contribution in each pixel from different blended sources. Therefore in deblending, each pixel can belong to more than one object. Deblending is more realistic: the sum of the light profiles of multiple overlapping objects specifies the final pixel value. However, to be accurately done, deblending will require parametric analysis and fitting algorithms. Segmentation, on the other hand, is a very low-level measurement and only goes so far as to assign each pixel to the sub-component that contributes most to it. Therefore segmentation provides the best starting point for the higher level deblending if it is needed.¹⁰ NoiseChisel will not do deblending but only performs segmentation.

In order to segment each detection into sub-components, *clumps* (Section 3.2.1) and *objects* (Section 3.2.2) are defined. A detected region might contain one or more objects and anything from none to multiple “true” clumps. Finding the clumps in an object or detected region is a low-level measurement that provides us with a multitude of false clumps mixed with possibly true clumps. True clumps can be found robustly by studying the noise properties in the vicinity of the detected regions. This process is very similar to how true/false detections were separated in Section 3.1.5. In Section 3.2.1 the proposed definition for a clump and the true/false classification is explained. The segmentation of a detected region to objects is a high-level measurement thoroughly discussed in Section 3.2.2.

3.2.1. Finding “True” Clumps

Pixels at a local maximum are defined as those whose value is larger than their 8 connected neighbors. The 8 connected re-

¹⁰ We will be working on such a fitting tool for deblending as part of the GNU Astronomy Utilities to start using the outputs of NoiseChisel.

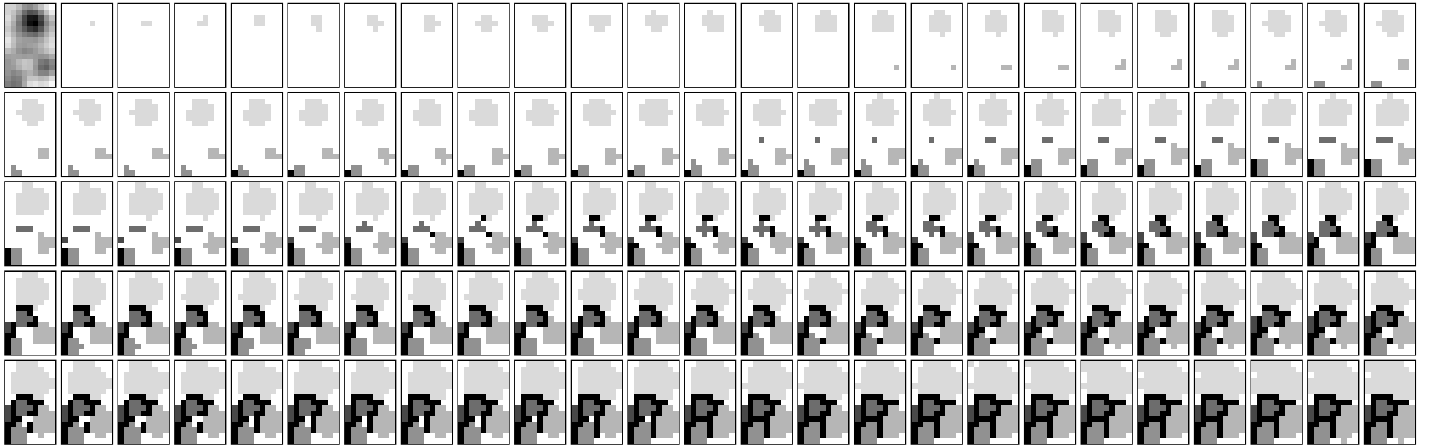


Figure 8: Pixel-by-pixel demonstration of oversegmentation (see Section 3.2.1 for a complete explanation of the algorithm). The order is from the top left to the bottom right. First: a small region in the center of Figure 9(b.2). The rest show how pixels are labeled in order of their value. The shades of gray become darker as the labels increase. The darkest shade of gray represents river pixels.

gion around each local maximum whose pixels all have a lower count than the peak is defined as a *clump*. Note that the clump can be much larger than 9 pixels.

The approach introduced here for finding the clumps associated with all the local maxima of an image is conceptually very similar to and inspired by the method proposed by Vincent and Soille (1991), without using layers because of the biases they produce (see the discussion in Section B.2). Figure 8 shows the process for 124 pixels of the central region of Figure 9(b.2).

A zero valued array with the size of the image is first created to store the labels of the different clumps. All the pixels of each object are ordered based on their value. Starting from the brightest pixel and in decreasing order, the pixels are labeled based on the following conditions.

1. If the pixel is not 8 connected to any other labeled pixels, it is a local maximum and is assigned a new label. This can be seen as new labels (darker shades of gray) are added in Figure 8.
2. If its 8 connected neighbors all have the same label, the pixel is given that label as well. In Figure 8, this occurs most often (when the colored areas expand).
3. If its neighbors have different labels, like a river flowing between two mountains,¹¹ the pixel is a local minimum. The *river* pixels act as separators of each mountain or clump. River pixels are the darkest pixels in Figure 8. The pixel-by-pixel construction of the rivers can be seen from the middle of the third row in Figure 8 as the growing regions start touching. In this setup the rivers are 4 connected. If 4 connectivity was chosen for checking neighbors, the rivers would be 8 connected.

The application of this simple algorithm to the non-detected regions of the image can be seen in column 3 of Figure 9 and

¹¹ As Vincent and Soille (1991, page 583) put it, “In the field of image processing and more particularly in mathematical morphology, grayscale pictures are often considered as topographic reliefs. In the topographic representation of a given image I , the numerical value (that is, the gray tone) of each pixel stands for the elevation at this point. Such a representation is extremely useful since it allows one to better appreciate the effect of a given transformation on the image under study.” In this analogy, the noisy image can be considered as a mountain range and when rain comes, the water gathers in the local minima of those mountain ranges to form rivers.

on the detected regions in column 5. Similar to our discussion in Section 3.1.5, the region of no detection is used as a basis or calibrator to find the true clumps over the detected regions. This algorithm for finding the clumps uses their relative values. Therefore as discussed in Section 3.1.1, the convolved image is used to find the index of pixels in each clump. The small convolution kernel is beneficial for this step because the spatial resolution is very important for an accurate result. This pixel-by-pixel expansion process provides the ultimate usage of the dynamic range of the convolved image.

A very large fraction of the clumps found over a detected object (column 5 in Figure 9) are due to background and correlated noise. To identify the false clumps, the segmentation results on the noise regions of the image (column 3 of Figure 9) are used as a reference. As discussed in Section 3.1, it can be assumed with high certainty that there is no significant signal (from a true physical object) in the noise regions. Furthermore, the noise regions in the vicinity of the object would contain the same undetected astronomical objects and instrumental and data analysis biases as the object pixels. Therefore this region is the most accurate and objective reference available to judge between a true and a noise clump.

On the original unconvolved and not Sky subtracted image, F_i and F_o are respectively defined as the average count in a clump and on all river pixels surrounding it. The average value of the river pixels around each clump approximately show the base elevation or count if the clump was not present. Let N_i be the total area or number of pixels inside a clump. The S/N of each clump can be written as,

$$S/N = \frac{N_i F_i - N_i F_o}{\sqrt{N_i F_i + N_i F_o}} = \frac{\sqrt{N_i} (F_i - F_o)}{\sqrt{F_i + F_o}}. \quad (4)$$

See Section 3.3 for how this equation can be modified for images that are not in units of counts or have already been Sky subtracted. The S/N distribution of all the clumps in the blank Sky can be seen for all the examples of Figure 9 in column 4 of that figure. The --segquant=0.99 quantile of the distribution is used to find the S/N threshold to accept or reject a clump over the detected object. This threshold is thus completely independent of the particular object in which the potential clumps are embedded. Note that the criteria in SExtractor and some other existing

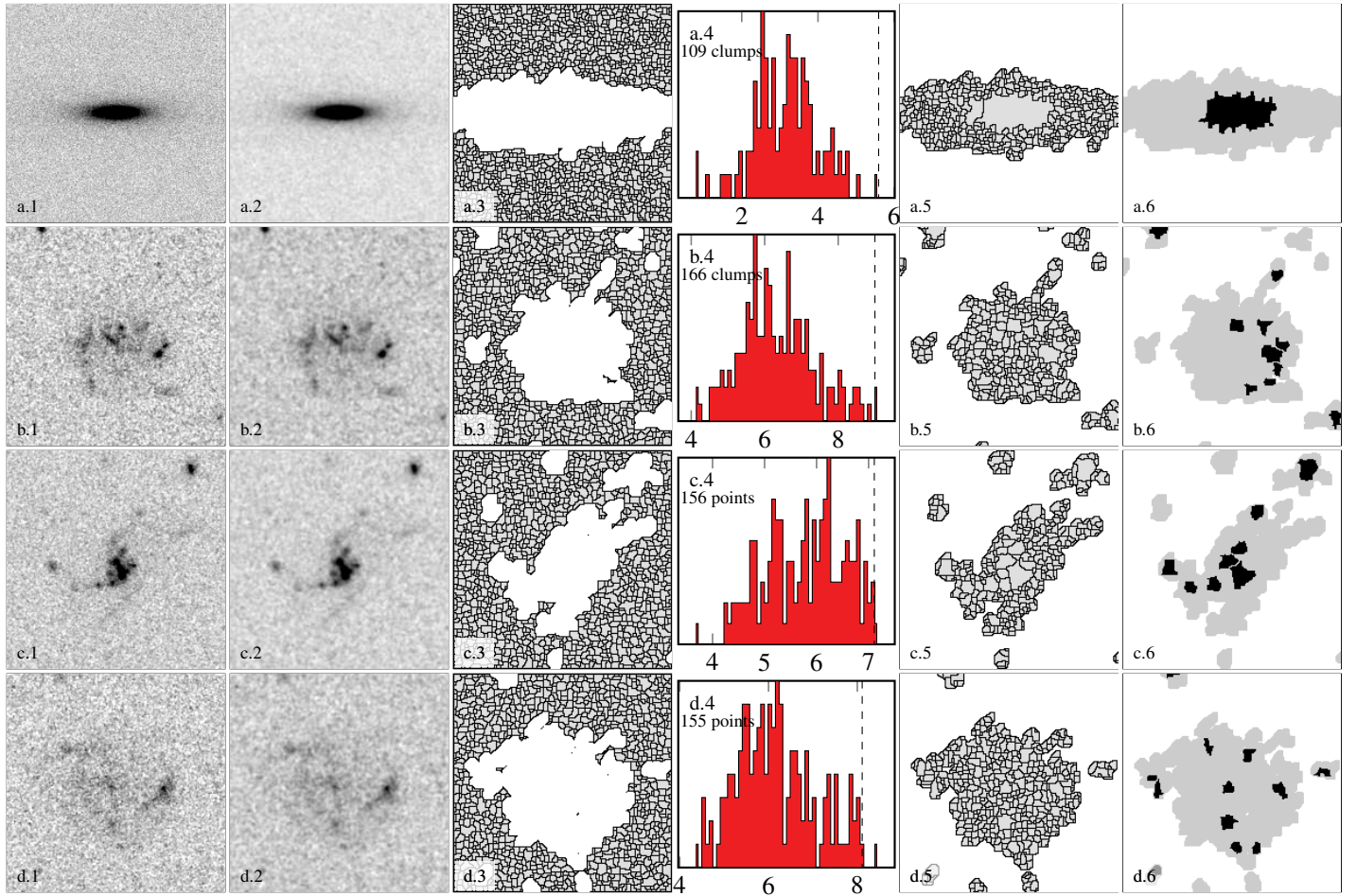


Figure 9: Finding clumps through oversegmentation. Column 1: input images. Column 2: convolved image (Section 3.1.1). Column 3: oversegmentation applied to non-detected regions on the convolved image. Column 4: signal-to-noise ratio histogram (Equation (4)) of all segments in column 3 with an area larger than `--segsnminarea=25`. The dashed line shows the position of the `--segquant=0.99` quantile. Column 5: oversegmentation applied to the central object. Column 6: clumps in all the detected objects with signal-to-noise ratio larger than the threshold of column 4. Note that some detections have no true clumps.

tools for deblending an object is the fraction of counts in each clump to that in the parent detection (see Section B.2 for a discussion of the resulting biases). Since no layering is necessary and the clump counts are not compared to the object anymore, the clumps in various galaxies can now be objectively compared with each other.

Since the average count in each clump is very important in the S/N calculation, only clumps having an area larger than `--segsnminarea` are considered in the comparison. Any clump that is smaller than this area will be discarded as noise. For the examples in this paper it is set to 25. This is larger than `--detsnminarea`, because the areas there were found by applying a threshold to the input image, while the clumps here are found on the convolved (smoothed) image where the areas become larger. Clumps smaller than this area add very strong skewness to the S/N distributions.

3.2.2. Object Segmentation

The very low thresholds that were used (see Section 3.1.2) cause objects that are close enough to each other on the image to be blended in one detection. Three real examples are displayed in the first column of Figure 10. The basis for separating potential objects in a given region is the true clumps which have been found in that detection. Therefore, if a detected region has

none or only one clump, it is considered to be only one object. If there is more than one clump in a detected region, the clumps are grown until a certain threshold of the input image. If the Sky value (average of non-detected pixels) and its standard deviation are labeled with S and σ_s , then the threshold to stop clump growth is $S + g_{\text{thresh}} \times \sigma_s$. In the examples of Figure 10 it is set to `--gthresh=0.5`.

The process of growing the clumps is very similar to the algorithm in Section 3.2.1 (Figure 8) with the exception that no new labels are added. If a pixel has no labeled neighbors, it is kept in a queue to be checked on a next loop. The loop continues until no new pixel can be labeled. The grown segments of each clump of the examples in Figure 10 can be seen in column 3.

Objects are defined based on the average S/N of the river pixels between the grown clumps of Figure 10, column 3. Two grown clumps are defined as separate objects if the river between them is below a user-defined S/N. If it is larger, then the connection between the grown clumps is too strong to be regarded as separate objects. Therefore the grown clumps are considered as parts of one object. Let F_{ij} represent the average count on the river between the grown clumps i and j . The average S/N of the river between these two clumps is defined as:

$$S/N_{ij} = \frac{F_{ij} - S}{\sqrt{F_{ij} + \sigma_s^2}}. \quad (5)$$

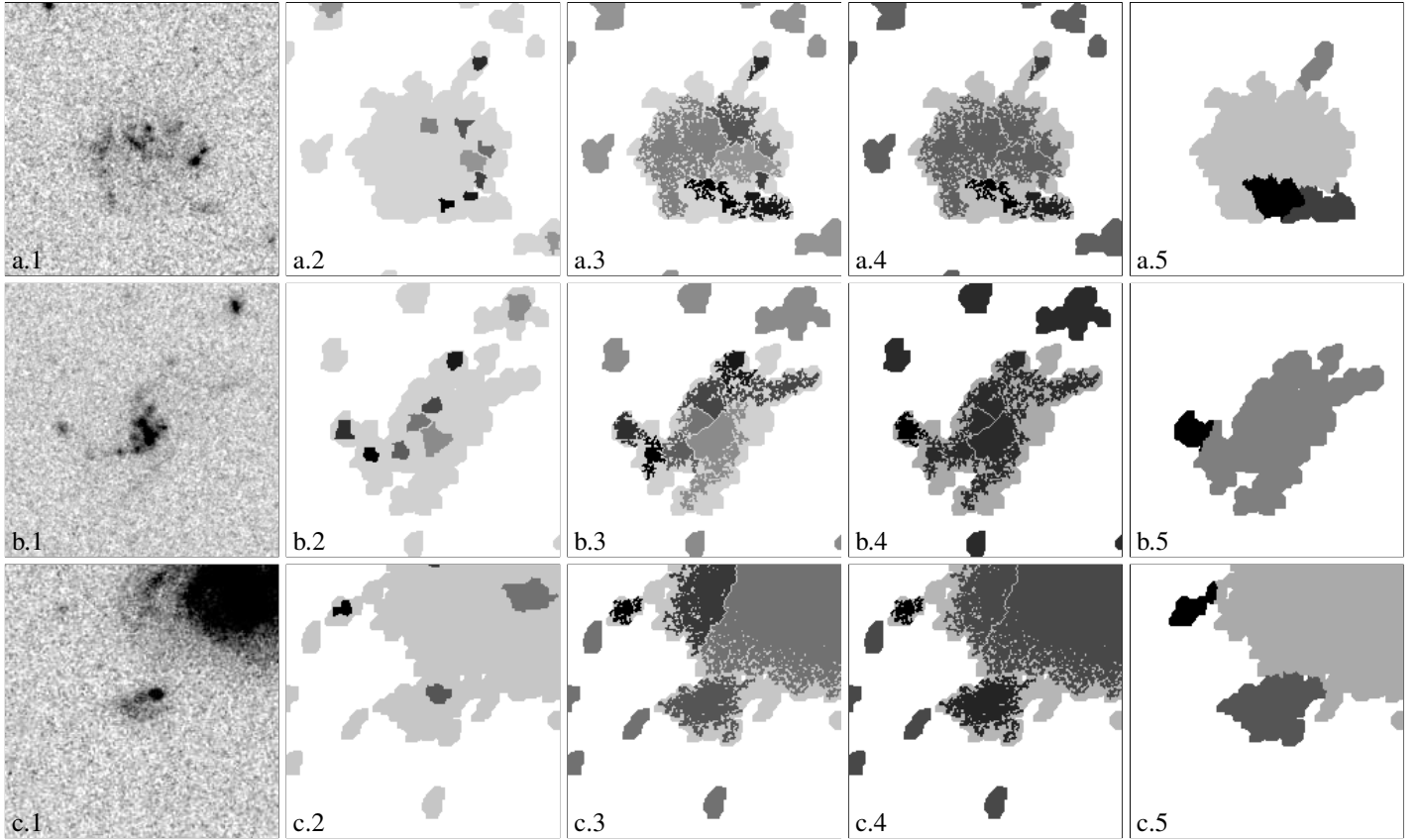


Figure 10: Segmenting objects. Column 1: actual images. Column 2: true clumps in the detections (see Section 3.2.1). Each clump is color-coded based on its label. The underlying light gray region shows the detection region. Column 3: the clumps are grown until $--gthresh=0.5$ (see Section 3.2.2). Column 4: all objects with boundary signal-to-noise ratio larger than $--objbordersn=1$ are given the same label. Column 5: the remaining pixels of the region are filled by growing the labels of column 4. In the last column only the central segmented objects are shown for clarity.

If $S/N_{ij} < objbordersn$, then these two grown clumps are considered separate objects and if not, they are defined as belonging to the same object. In the examples of Figure 10 this is set to $--objbordersn=1$. $S/N_{ij}(=S/N_{ji})$ is calculated for all the grown clumps of each detection. Finally, all the clumps that are connected to each other within a detection are given one label (see column 4 of Figure 10). Note that if two grown clumps have $S/N_{ij} < objbordersn$, and they are both connected to a third clump with $S/N_{ik} > objbordersn$ and $S/N_{jk} > objbordersn$ then all three grown clumps will be given the same label. The rivers between two grown clumps are only one pixel wide. Therefore in the calculation of F_{ij} , the count of each pixel is taken as the average of that pixel and its 8 connected neighbors. Hence, in practice the rivers between two grown clumps are 3 pixels wide.

Because of the absolute nature of the two parameters for object definition (as opposed to the relative nature in the case of detection and clumps), namely the user directly providing $--gthresh$ and $--objbordersn$, the object definition is not robust and objective like that of detections and clumps. In fact $--objbordersn$ is the only user given S/N value in NoiseChisel.

The definition of objects made here is purely based on the one image input to NoiseChisel. The example above shows that this definition of objects is fundamentally subjective (directly determined by the particular data-set and the user and not necessarily based on physical reality). Two galaxies at vastly different redshifts might be sufficiently close to each other, on the same line of sight, that they are each defined as clumps in one larger object. However, due to surface brightness limits, the connection

(for example, through a spiral arm or a tidal tail) of a real star-forming region of a galaxy might not be detected. Therefore that region will be identified as a separate object. This also applies to rings and filaments. In order to solve these issues, the information in one data set (image in this case) is not sufficient, and ancillary data, for example, from spectroscopic data or images in other wavelengths, will be necessary. Therefore the physical reality of the ‘objects’ defined here is beyond the scope of any analysis based solely on one image.

3.3. S/N Equation Modifications

The standard deviation of the non-detected regions (σ_s), incorporates all sources of error: Poisson noise, read-out noise, etc. Hence, if the image is in units of counts and the backgrounds are not already subtracted once, then Equations (3) – (5) can be used no matter if the noise is background-dominated or read-out-noise-dominated. However, input images do not necessarily satisfy this condition. For example, the *HST*/ACS images shown above are processed (already Sky-subtracted) and distributed in units of counts per second.

When the image is in units of counts s^{-1} , and if the noise is background-dominated, all the terms in the equations have to be multiplied by a constant in units of time. In finding true detections and clumps that depend on the quantile of the S/N distribution, the absolute value of this constant makes absolutely no difference. However, in identifying objects, it is important, because the user specifies an absolute S/N value for rivers. NoiseChisel

will automatically detect if an image is in units of counts or counts s^{-1} using the minimum standard deviation in all the meshes (see Section 4). If this minimum is larger than unity, then it is assumed that the image is in units of counts. If not, the inverse of this minimum (which has units of time) will be used as the time constant discussed above.

If the input images are processed, then Sky subtraction has already been applied. Therefore the error in the average count F in the denominators should be $F + \sigma_s^2$, not F alone as is currently present in the equations. It is up to the user to specify this condition through the `--skysubtracted` parameter (see the manual for more details).

4. LARGE (REAL) IMAGES

Real astronomical images are not as small and clean as the examples in the figures in Section 3. They are often much larger or might contain masked pixels. The former often causes variations in background and noise (see Figure 11). These gradients do not necessarily have to be created by the background, but they might be due to processing, for example, bad fittings in flat fielding. Even if the image is very clear, and the targets are already accurately defined, the statistics when using such small postage stamps will not be accurate. By statistics we mean the number of false detections and clumps in the non-detected region that go into calculating the S/N quantile; see Section 3.1.5 and 3.2.1. Therefore much larger postage stamps, for example, from surveys, have to be used. As discussed in Section 2.1, the input FITS images of all the figures so far were much larger than those shown here.

The image is considered to be a grid of meshes. All the steps explained in Section 3 can be applied independently on each mesh. Since the operation on each mesh is completely independent of the rest, parallel processing can be applied to significantly improve processing time. This is only possible because all the methods in NoiseChisel are non-parametric.

Some procedures are directly linked to the potential gradients in the image, for example, convolution (Section 4.1), thresholds (Section 4.2.1), and Sky subtraction (Section 4.2.2), while others are only defined after the gradients have been removed and need a large area for statistical accuracy, for example, removing false detections (Section 3.1.5) and finding clumps (Section 3.2.1). To be able to adequately do both jobs, two mesh sizes are defined: a small mesh specified by `--smesh` for the former class of operations and a large mesh specified by `--lmesh` for the latter. Each specifies the sides of a square mesh. As explained in Section 2.1, in the examples of Section 3, `--lmeshsize=200` (so one mesh covers the displayed postage stamps) and for Figure 11 it is set to 256. In all the examples of this paper, `--smeshsize=32`.

4.1. Convolution

Image convolution is mostly done using the discrete Fourier transform in the frequency domain (see Gonzalez and Woods 2008). When the convolution kernels are large, for example, when the image PSF is used, this technique provides significant performance benefits. However, it fails on the edges of the image. Spatial domain convolution, on the other hand, can be corrected to account for the edge effects or masked pixels and when the kernels are small it can be even faster. The kernels in

NoiseChisel are small so added to its extra capability, spatial domain convolution is used (see the Convolve section of the GNU Astronomy Utilities manual for a complete explanation).

4.2. Interpolation and Smoothing

Some meshes will not be able to provide an input in the grid, for example, because of a large object that is larger than the mesh. Therefore interpolated values will be used for unsuccessful meshes, and finally, the mesh grid is smoothed. We will discuss the case for the quantile threshold (Section 4.2.1) and Sky value (Section 4.2.2) more accurately here.

Following the non-parametric nature of NoiseChisel, functional interpolation techniques like spline or cubic interpolation will not be used. They can result in strong outliers on the edges or corners like those in Figure 16(a)–(c) and (l). To interpolate over each blank mesh, the median value of the nearest `--numnearest` acceptable meshes is used. The nearest non-blank neighbors are found efficiently through a breadth-first search strategy in graph theory. In such a median interpolated grid, the result will not be smooth. Hence an average filter¹² is applied to the interpolated grid to make smoother variations between neighboring meshes. The final interpolated grid for the Sky value can be seen in Figure 11(c).

4.2.1. Threshold

The quantile threshold of Section 3.1.2 can only have a comparable value between all meshes, if the signal in the mesh is not significant compared to the noise. Otherwise, with more signal contributing to the mesh, the pixel distribution in the mesh will become more skewed and thus the quantile value found will also shift and not be comparable between different meshes. In order to find the threshold, the novel algorithm of Appendix C is used to find the mode of the image. The mode acts as a gauge for the amount of data that is mixed with the noise in that mesh.

With more signal contributing to the mesh, the average, median, and mode will shift (with decreasing rates) to the positive (see Figure 1 and Appendix C). Exploiting this property, the significance of signal in noise of a mesh regardless of its morphology can be assessed using the difference between the median and the mode such that the closer the mode is to the median, the less significant signal there is in the mesh. Through the parameter `--minmodeq`, the user can set the minimum acceptable quantile for the mode. In this paper it is 0.49. Note that the skewness induced by convolution, further skews the distribution, or, distances the mode and median (see Section 3.1.1 and Figure 4). Hence the 0.49 value is a very strong constraint.

4.2.2. Sky and σ_{sky}

As defined in Section 2.2, the Sky value is the average of undetected pixels in each mesh and its error is their standard deviation. Figure 11(a) shows an example Subaru Telescope SuprimeCam image that has undergone initial processing after flat fielding and prior to Sky subtraction. The visible gradients in the input image are most probably due to problems in flat fielding rather than actual variation in the Sky. Finding the cause

¹² The value of each mesh is replaced with the average of it and its 8 connected neighbors (see Figure 6(b)).

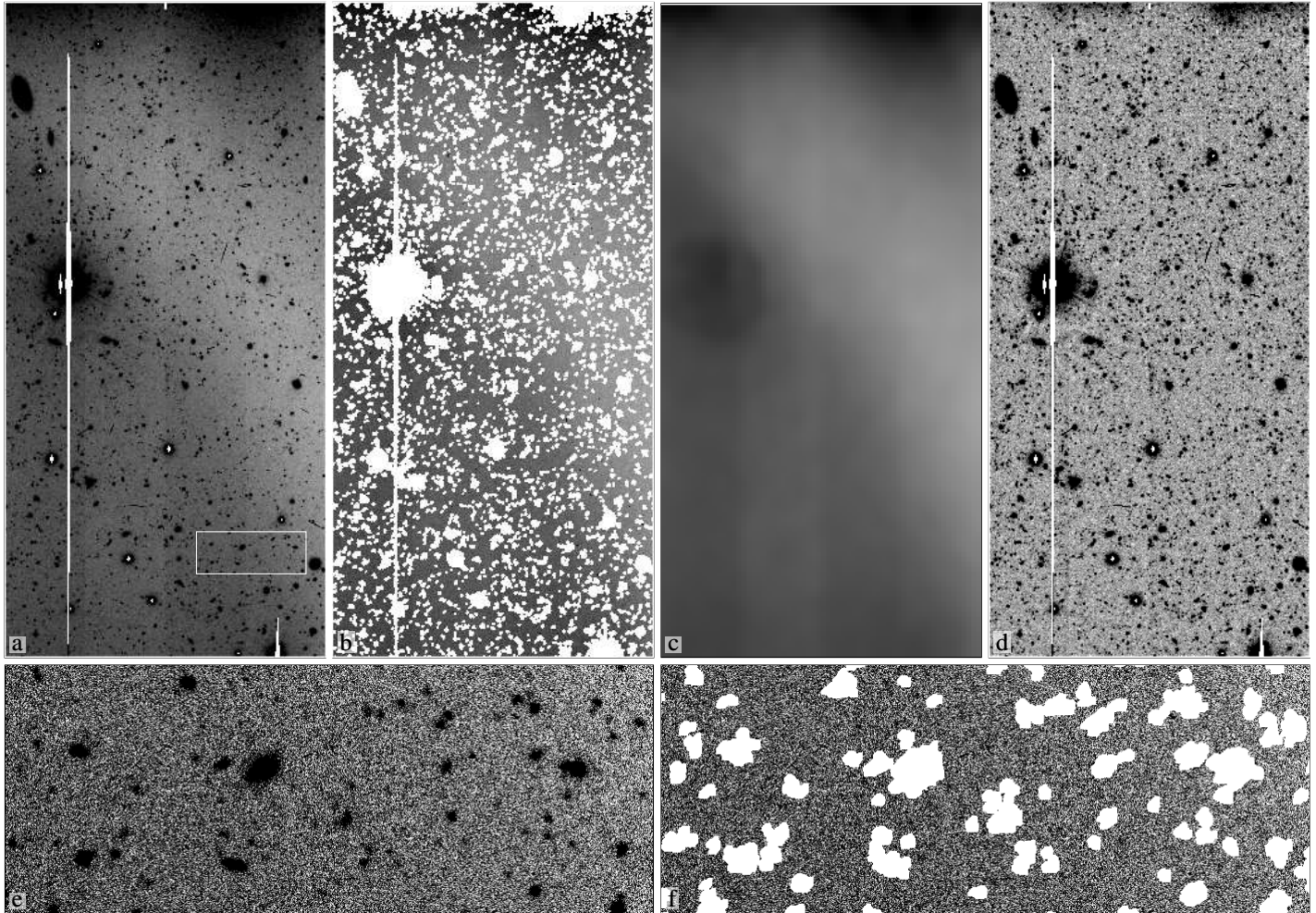


Figure 11: Applying NoiseChisel on a raw image prior to Sky subtraction from Subaru SuprimeCam. The image is 2048×4177 pixels. (a) The raw image after bias subtraction, dark subtraction and flat fielding have been applied. (b) All the detected regions in the image have been removed to expose the Sky. (c) The interpolated and smoothed Sky value defined as the average of undetected regions over a mesh grid. (d) The Sky value on each mesh is subtracted from the respective region of the image. Notice how the gradients in the input image have been mostly removed. (e) Enlarged image of white box in (a). (f) Zoom-in of the same region in (b). The color truncation values in (a)–(c), (e), and (f) are exactly the same; for (d) they were set such that the bright star has the same apparent diameter. The white pixels in (a) and (d) are masked pixels.

of this gradient is very important, but beyond the scope of this paper. No matter how it was created, a good detection algorithm has to be as resilient to such gradients as possible. This particular image was intentionally chosen to demonstrate NoiseChisel’s ability to account for such gradients.

Figure 11(b) shows the detected objects removed from the input image. The image is covered with a mesh grid of size `--smesh`. The Sky on each mesh is found from the average of the undetected pixels in that mesh. Only those meshes with a sufficiently large fraction of undetected pixels are used. If too much of the mesh area is covered with detected objects, that mesh will not be used because of the potential fainter wings penetrating to the undetected regions; compare Figures 3(a.1) and (a.8). The fraction can be set by `--minfrac`, in this paper it is set to 0.5.

Cosmic rays can be a problem for determining the average and standard deviation. For example, long exposures in raw *HST*/ACS images are heavily peppered with cosmic rays (see Figure 15 for a normal example). Since cosmic rays are very sharp and can be very small, some will not be detected by the detection algorithm. Therefore a simple calculation of the average and standard deviation will be significantly biased if cosmic rays are present. To remove the effect of cosmic rays, σ -clipping with

the same convergence-based approach as SExtractor is used (see Section A.3). Note that by this step the mode and median are approximately equal, so that σ -clipping is just used to remove the effect of cosmic rays on the average and standard deviation.

The interpolated and smoothed (see Section 4.2) Sky map can be seen in Figure 11(c), each pixel in this image represents a 32×32 pixel mesh. Finally in Figure 11(d), the Sky value for each mesh is subtracted from the pixels in that mesh. The gradients and differences between the different CCD chips have been significantly suppressed. Notice that even with this small mesh size some of the strong top right gradient still remains.

5. ANALYSIS

NoiseChisel is based on detecting an object deeply buried in noise using its fainter parts (see Section 3). In contrast, existing techniques rely on detecting the brightest regions and growing those (based on a priori models) to include the fainter parts (see Appendix B). Hence these methods are fundamentally different. The detection accuracy is analyzed here using three fundamental and basic statistics that can be done with mock profiles in mock noise. Comparing the Sky and background value when the latter

Figure Label	Median	Mode	σ -clip Converge	σ -clip (4,5)	SExtractor Average of Undetected	NoiseChisel Average of Undetected	NoiseChisel N_f (Section 5.2)
12(a) and 18(a)	5.6	5.7 ^{LS}	5.4 ± 99.9	5.6 ± 99.9	5.1 ± 99.9	2.2 ± 99.2	3
12(b) and 18(b)	6.6	6.6	6.4 ± 100.7	6.6 ± 100.7	5.9 ± 100.7	3.5 ± 100.1	4
12(c) and 18(c)	4.8	2.2	5.6 ± 101.2	4.8 ± 101.2	3.9 ± 100.5	3.1 ± 100.4	2
12(d) and 18(d)	5.9	5.9	6.3 ± 102.2	5.9 ± 102.2	3.1 ± 100.4	2.2 ± 100.1	2
13(a) and 19(a)	3.4	1.3	5.1 ± 29.0	3.1 ± 28.6	-0.9 ± 25.0	-1.2 ± 25.0	N/A
13(b) and 19(b)	2.0	0.7	3.1 ± 27.9	1.9 ± 27.8	-0.7 ± 25.8	-0.8 ± 25.9	N/A
13(c) and 19(c)	2.1	0.7 ^{LS}	2.5 ± 22.0	1.6 ± 21.7	-0.9 ± 19.7	-1.1 ± 19.8	N/A
13(d) and 19(d)	4.1	3.0	5.2 ± 28.6	4.1 ± 28.5	-1.1 ± 25.5	-1.2 ± 25.6	N/A
13(e) and 19(e)	38.9	32.3	41.1 ± 115.8	36.1 ± 114.9	23.7 ± 102.8	8.3 ± 100.2	3
17(a)	20.2	9.5	23.1 ± 114.2	17.1 ± 113.1	8.3 ± 100.9	1.8 ± 99.9	3
17(b)	S/A	S/A	S/A	S/A	6.9 ± 100.7	S/A	S/A
17(c)	S/A	S/A	S/A	S/A	5.3 ± 100.3	S/A	S/A
17(d)	S/A	S/A	S/A	S/A	-5.0 ± 99.9	S/A	S/A

Table 1: Sky value on the figures in units of counts. counts s^{-1} data multiplied by $10^4 s$. For mock images, the background ($= 10000e^-$) was subtracted. *LS*: low symmetry, see Appendix C. S/A: same as above. N/A: not applicable.

is accurately known (in a mock image) is the most basic test to evaluate the success of a detection algorithm. This comparison is done in Section 5.1. Purity is a quantitative measure to assess the contamination of false detections that remain in the final result. In Section 5.2 purity is defined and used for an analysis of false detections in the faintest limits. Finally, in Section 5.3, the faint end magnitude dispersion is studied. The statistical significance of the imposed requirements on the objects detected as true is discussed in Section 5.4.

While being demonstrative for a “proof-of-concept” paper like this one, tests using mock objects or noise can never simulate all real circumstances accurately. Thus NoiseChisel is tested using only real data without any modeling in a companion paper by M. Akhlaghi et al. (2015, in preparation). Its accuracy is further evaluated, for example completeness, purity, number counts and etc on real data in that work. The details of the real data set, necessary modifications to the existing pipeline, tests, and an analysis of their results is beyond the scope of this definition or “proof-of-concept” paper.

5.1. Sky Value

The Sky is the average of undetected regions. Therefore the success of a detection algorithm can be assessed with the effect of undetected objects on the Sky value. The more successful the detection algorithm is, the closer the Sky value will be to the background value, which is $10000e^-$ for all the mock images (see Section 2.2). There are two types of “faint” pixels that can be left undetected. (1) When the brightest pixels of an object are faint, for example, Figure 3(c.2). (2) When the object is bright enough to be detected but has wings that penetrate into the noise very slowly (for example Figure 3(a.2)). The failure to detect both will be imprinted into the average of undetected regions of the image.

Table 1, has all the relevant data for this comparison. Except for the last column, all columns in Table 1 show the pixel statistics of images shown in the figures of column 1. In these statistics, only the pixels within the 200×200 pixel box are used and not the whole image (see Section 2.1). As σ -clipping is still extensively used in existing pipelines (see Section A.3) in Table 1 the results of the two major σ -clipping strategies are also included, by convergence and (4,5). In SExtractor, which uses the former, the average is used as the Sky value and in the latter, the

median is used, so we take the same approach here.

The σ -clipping results show that due to the skewness caused by galaxies (which do not have a sharp cutoff), none are significantly different from the median. Since the final average is used in the former, its reported values can be even larger than the initial median. The correlated noise, which acts like a convolution and skews the distribution, causes this difference with the mode to be much larger in the real (processed) images of Figures 13 and 19 (a)–(d) than the mock images.

In order to check the sensitivity of NoiseChisel, it is applied to a set of mock and real images of Figures 12 and 13 with the default parameters discussed in Section 3 and Section 4 and fully listed in Appendix E. The values for the Sérsic index in Figure 12 ($n = 0.5, 1, 4$ and 10) were chosen to approximately cover the range of observed galaxy profiles (for example, see Lackner and Gunn 2012). The objects in Figure 13 are *HST/ACS*, F814W images from the COSMOS survey of what are thought to be three $z \sim 1.5$ star-forming galaxies, so that they are imaged in rest-frame UV. The same input images are given to SExtractor (Figures 18 and 19 in Appendix B with the configuration file shown in Appendix D) and the results are reported here. Some studies use the average of undetected pixels when SExtractor’s detections have been removed. Therefore in column 6 of Table 1 the average pixel value when all SExtractor detections have been masked to $3, 3.r_k$ is reported.

The mock images (with a number in the last column) show that compared to σ -clipping, removing SExtractor’s detected objects has been more successful in approaching the real background value ($0e^-$), but the average of the undetected regions are still a significant overestimation. The last 4 rows of Table 1, which successively mask more of the bright profile, show that this is not only due to undetected objects, but also the fainter parts of bright objects. The last row shows that when too much of the image is masked, the average of non-detected pixels goes below the real Sky value. This is reasonable because localized high valued noise pixels are systematically removed.

Over-estimating the Sky value results in a systematic underestimation of the total count of the detected objects. In the most diffuse and low surface brightness cases, a severe Sky overestimation can even result in a negative total count for the targets. Some of the individual pixels of a real object can be below the Sky value (Section 3.1.2) but if the Sky value is accurately found, the total count of a real detection can never be negative. If it oc-

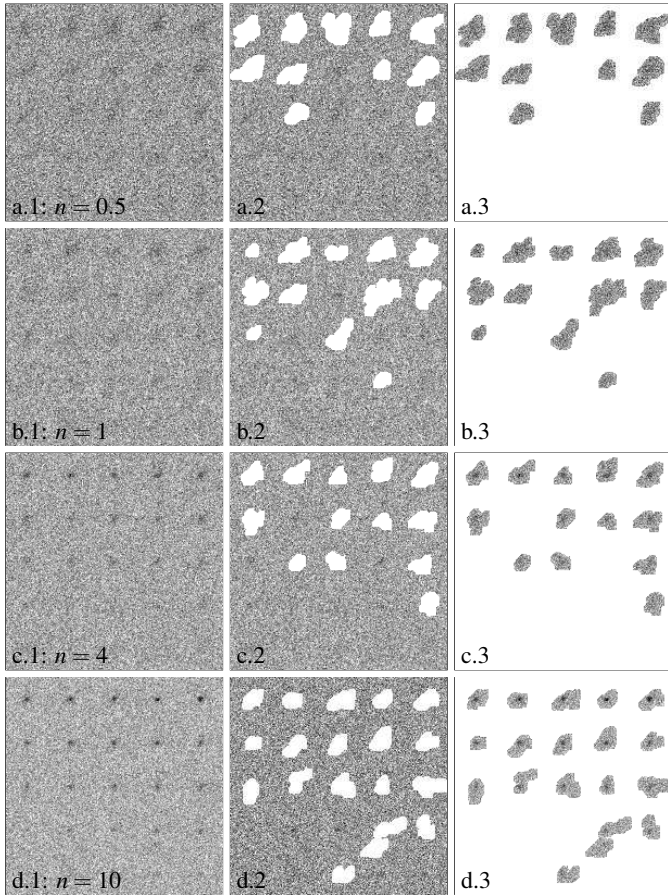


Figure 12: NoiseChisel sensitivity test. In each image there are 25 mock profiles, equally spaced (see Figure 3(b.1) and (c.1) for the images prior to adding noise for the cases of $n = 4$ and $n = 1$). Except for their total magnitude, all profiles in each image have the same parameters, $r_e = 10$ pix, $\theta = 45^\circ$, $q = \text{seq}$. The Sérsic index in each input image is different. The profiles on the bottom left are the faintest with -9.2 magnitude while those on the top right are the brightest with -10.64 magnitude. The second column shows the regions of the detected objects masked from the input image. The third column is the inverse of the second.

curs, it can only be due to the overestimation of the Sky. This problem can only occur in the existing signal based approach to detection where any pixel above the threshold is assumed to be the top of a profile. Negative total counts have been reported and extensively used in the SDSS survey, for example. However, only the problem of not being able to measure the logarithm of a negative value (for conversion to a magnitude) was addressed (see Lupton et al. 1999). The source of the problem, which is an overestimation of the Sky, was not sought. In NoiseChisel, if the numerator of any of the S/N measurements (Equations (3)–(5)) becomes zero or negative, that detection, clump, or river is discarded.

For the mock galaxies, where the background is accurately known, when the area covered by a diffuse source is the greatest (Figures 12(a), 13(e) and 17(a) and (b)), NoiseChisel’s detection algorithm is 2.3, 2.9, 4.6, and 3.8 times more successful than SExtractor.

For Figures 13(e) and 19(e), Table 1 shows the edge and crowded field effects on both SExtractor and NoiseChisel. Compared to the other mock images, NoiseChisel’s Sky value is systematically higher in this case. This is not due to the edge but due to the six large $n = 4.00$ profiles that exist in this image (see Figure 1 (b.1) for the complete pixel coverage of one of those six

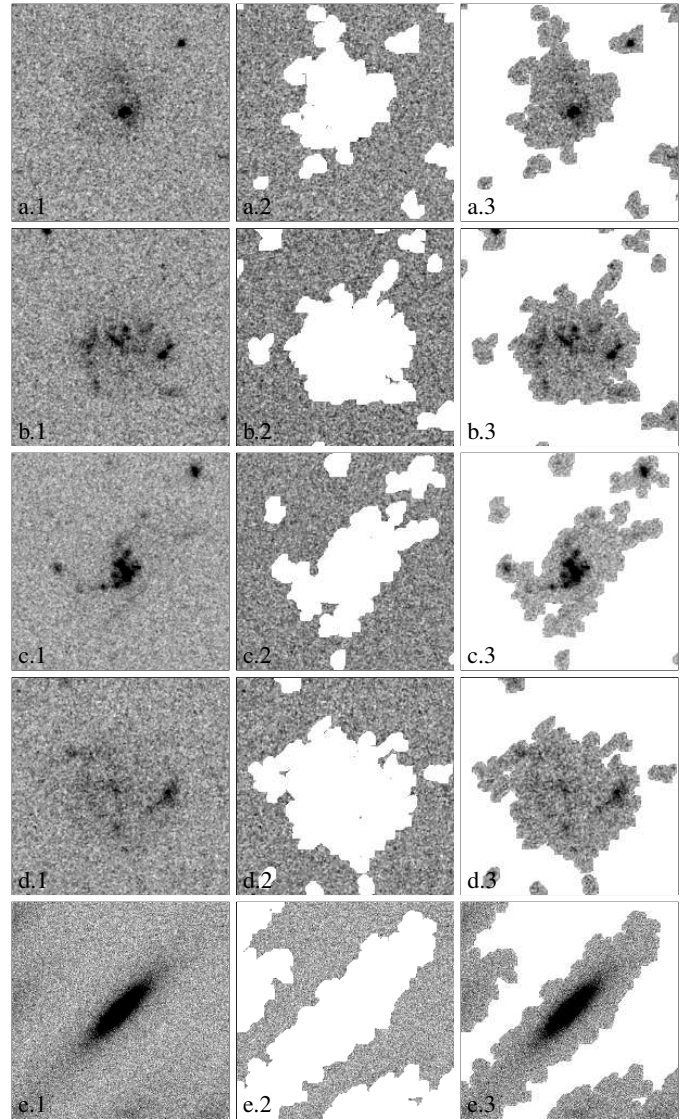


Figure 13: NoiseChisel applied to realistic conditions. (a)–(d) Four real galaxies. (e) Six mock profiles with the same parameters of Figure 1(b) and position angle of $\theta = 45^\circ$. Five of the profiles are centered 35 pixels outside the bottom and left edges of the image; see Section 2.1. The columns are the same as those in Figure 12. The truncation count (where black pixels are defined) in (e.1) is half that of Figure 1(b) to emphasize the faint wings of the profiles outside the image edge.

profiles). If `--smesh` was set to a larger size to find the threshold (see Section 4.2.1), the meshes covered by the objects would be ignored and NoiseChisel’s final Sky value would be lower. However, Figure 11(d) shows that even such a small `--smesh` was not enough to completely remove some strong gradients. Therefore this higher Sky value can be corrected if there are no gradients in the image. Only one value for the full displayed region was discussed here. In practice, SExtractor interpolates over such regional values to find a background value for each pixel. Section A.6 discusses the process and shows the histogram of the pixel by pixel Sky values used.

5.2. Purity

Assume that we have made mock profiles in mock noise where the number and positions of the mock objects buried in the noise are already known. By construction we know there

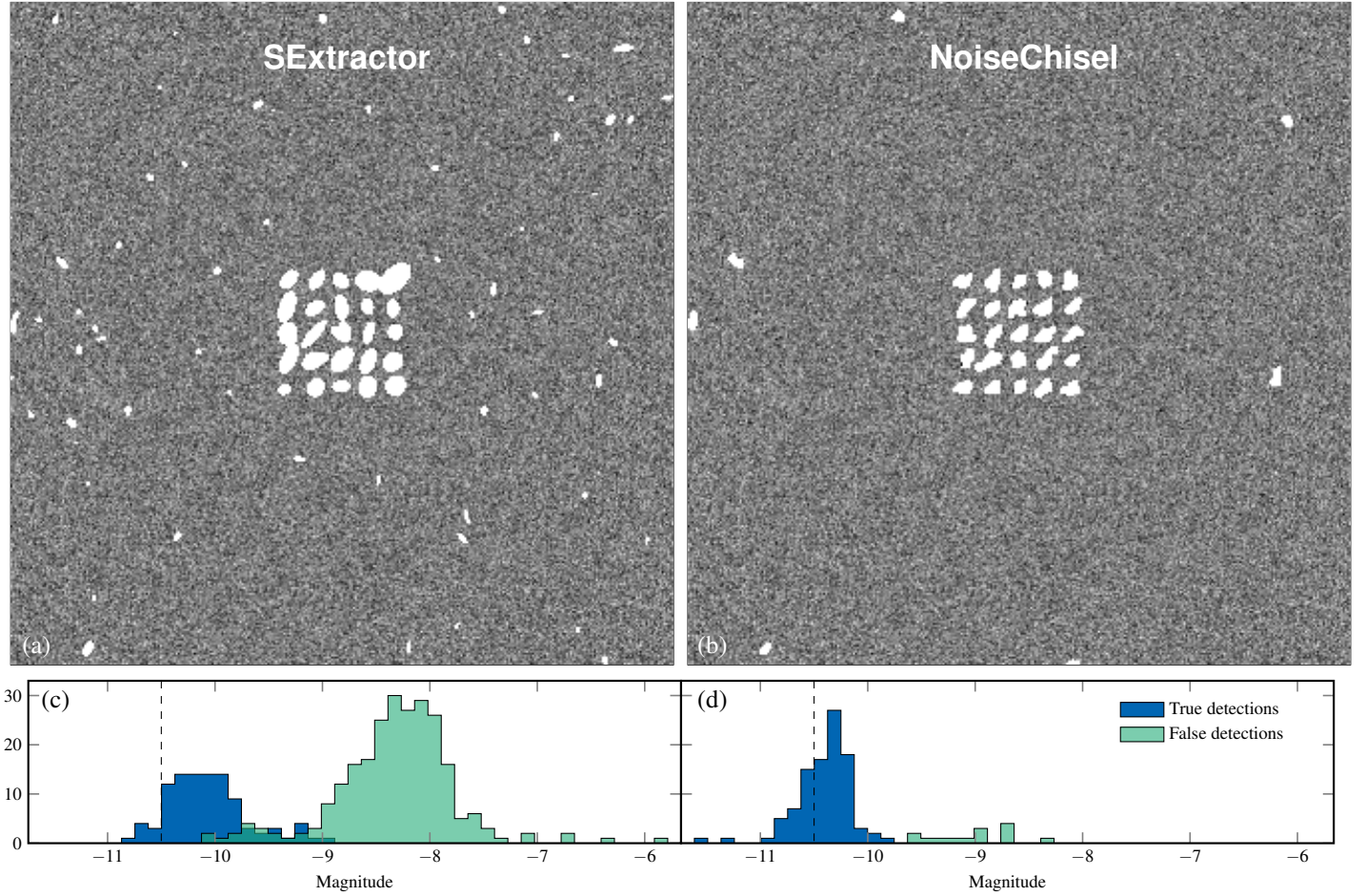


Figure 14: Comparison of purity (false detections) and dispersion in measured magnitude when completeness is 1 for identical and very faint $n = 0.5$ profiles. (a) and (b) 25 profiles are located in the central 200×200 region, so any detection outside of it is false, see Section 2.1. Completeness is constrained to 1 for both techniques. SExtractor and NoiseChisel have 69 and 7 false detections respectively. The two histograms (c) and (d) show the distribution of magnitude (with zeropoint magnitude of 0) for the true and false detections for the respective technique. The dashed line shows the true magnitude of all the profiles. The histograms are derived from four runs (100 true detections) on an identical no-noised image but with different simulated noise seeds. (a) and (b) had the most number of false detections for each method.

is no other source of signal in such an image. Take N_f to be the number of false detections, N_t the number of true detections, N_T the total number of detections, and N_I the total number of input mock profiles. Therefore $N_f + N_t = N_T$. The completeness, C , and purity, P , of a given detection algorithm with a given set of parameters are defined as

$$C \equiv \frac{N_t}{N_I}, \quad P \equiv \frac{N_t}{N_T} = 1 - \frac{N_f}{N_T}. \quad (6)$$

Completeness is commonly measured with mock profiles, for example, mock point sources or mock galaxies. The results from such mock objects are not realistic. This is because, as discussed throughout this paper, real galaxies display very diverse morphologies and do not generically satisfy the clean elliptical and radial profiles that can be modeled. Therefore any result based on mock objects will overestimate C . When the detection algorithm also depends on profiles having simple shapes with a clearly defined center and radially decreasing profile, the systematic bias is exacerbated. Purity, on the other hand, deals with false detections which don't require modeling.

Without true detections, purity will be 0 since $N_t = 0$ or $N_f = N_T$. In general, for a given set of parameters in any detection algorithm, C and P are anti-correlated: as purity increases, completeness decreases and vice versa. Therefore neither can

be studied independently. For example, in SExtractor decreasing the threshold in Figure 18 will allow the detection of more of the faint mock profiles therefore increasing completeness. Simultaneously, however, the number of false detections will increase (see Figure 17, for example) and thereby decreasing the purity of the output.

The methodologies of NoiseChisel and SExtractor are fundamentally different, therefore comparing their purity should be done carefully. To have a reasonably objective measure of purity in this case, the only way is to constrain completeness between the two. Therefore a mock image that has $C = 1$ with the default parameters of NoiseChisel is created. All the parameters of SExtractor are fixed to Appendix D, except `DETECT_THRESH` which is decreased until $C = 1$ is achieved in SExtractor too. This strategy is chosen based on the advice of SExtractor's manual to keep the sensitivity only related to `DETECT_THRESH`. The result will not be independent of the mock profiles used to define completeness. The sharper the profiles, the fewer faint pixels will be needed to reach $C = 1$. Hence an ideal test would be on the flattest profiles or those with $n = 0.5$, which both SExtractor and NoiseChisel show as their lowest completeness (see Figures 12 and 18).

To get an accurate measure of purity, a large area of the image has to have no data. The mock image is very similar to the input image of Figures 12(a.1). Recall that 96% of the area of

all the mock images in this paper is blank noise (Section 2.1). The only difference is that all 25 profiles have the same total -10.5 magnitude. This is done to decrease the effect of random noise positioning. The fixed magnitude of the mock profiles is set to be such that with the default parameters of Appendix E, NoiseChisel detects all 25 in the image. To make the test more robust, the mock noisy image is created four times, such that only the noise differs. The magnitude for all $25 \times 4 = 100$ profiles was the faintest magnitude that NoiseChisel would give $C = 1$ in all four images.

SExtractor could not detect all the objects without flagging some of their magnitudes as unreliable. So ignoring the flags, the largest threshold that SExtractor also gives $C = 1$ for all thresholds below it and for all four mock images is found to be `DETECT_THRESH=0.6`. The masked results of one of the images can be seen in Figure 14 once masked with SExtractor’s detections and once with NoiseChisel’s. In total, in the four images, 100 mock galaxies are present and in all four, completeness is 1. Therefore the result of all four images can be reported in one purity value for SExtractor (P_s) and NoiseChisel (P_n).

$$P_s = \frac{25 + 25 + 25 + 25}{79 + 90 + 94 + 87} = 0.29$$

$$P_n = \frac{25 + 25 + 25 + 25}{27 + 26 + 32 + 27} = 0.89$$

Even though the threshold used in NoiseChisel is so much lower than the smallest possible threshold to SExtractor (which is the Sky value), this result shows that the purity of NoiseChisel is about three times higher in detecting real, faint objects with the parameters used (see Appendices D and E). In the last column of Table 1 the number of false detections (N_f) in all the mock images is reported. Recall that like Figure 14, all mock images are also covered by Gaussian noise for 96% their area. With exactly the same input parameters, the reported N_f values agree well with those reported in this test.

As discussed in Sections 3.1.5 and 3.2.1, NoiseChisel is very robust in dealing with correlated noise that processed real images also have. However, SExtractor and all existing signal-based detection methods in general treat the pixels above the threshold as the top of a known profile; therefore they are not immune to the effects of correlated noise, resulting in lower purity when applied to a real processed image.

5.3. Magnitude Dispersion

All the profiles in Figure 14 are identical, however, Figure 14(a) displays a large dispersion in the shapes and areas in the detections. This results in the roughly 2 magnitude range that is visible in SExtractor’s true detections (see Figure 14(c)). It is very important to note that the bimodality that is observed in Figure 14(c) (ignoring color) is due to the fact that all mock profiles were identical. In a real image, the faintest true detections can have a variety of inherent profiles. Therefore the distribution will be unimodal with negative skew. The net result is a common plot in existing catalogs (for example see Figure 10 in Illingworth et al. (2013)). On the contrary, NoiseChisel’s true detections all have roughly the same area in Figure 14(b) and thus the range in the measured magnitude for true detections in Figure 14(d) is about half that of SExtractor. The two NoiseChisel

detections with magnitudes brighter than -11 are the result of four of the profiles being detected as two detections.

5.4. Imposed Restrictions on the Signal

The proposed algorithm imposes some restrictions on the objects it will detect as true. Therefore it is not “absolutely” noise based or independent of any signal parameter. Here we will discuss its methodological limits. With the chosen parameters in this paper (listed in Appendix E) the target has to satisfy the following conditions.

1. To be detected, an object has to have an area equal to or larger than Figure 6(c), above the initial quantile threshold (which is below the Sky value; see Section 3.1.2) on the convolved image.
2. To be classified as a true detection, it has to contain at least one connected component larger than 15 pixels above the Sky threshold with a sufficiently large S/N specified from the ambient noise (see Section 3.1.5) on the actual image.

As the methodological limits or requirements imposed on the target by a detection technique decrease, the detection algorithm becomes more successful because it becomes more generic. The “success” of a detection algorithm can be defined as how accurate its Sky measurement can approximate a known background, the purity of its result and the scatter in its photometry as discussed above. It was shown that because of far fewer constraints on the target objects, this technique was significantly more “successful” compared to SExtractor (with the parameters of Appendix D).

In astronomical data analysis, an S/N above five is usually considered as a “solid” result, any measurement with a lower S/N is usually included in an analysis with caution (McLean 2008, Section 1.5.2). Using ideal simulated noise we showed that objects and clumps with an S/N as low as 3.61 (Figure 7) can be accurately (0.99%) detected with this technique using this set of parameters. Note that the Sky value used in those plots was a first (under-estimated) approximation, therefore the counts and hence the S/Ns are overestimated. Hence the true limiting S/N is slightly less than what is reported in those plots.

Through setting fewer constraints (if a similar purity level can be achieved) it would be possible to decrease the S/N of true detections even further. The extreme case would be to detect objects with an S/N of unity. However, the statistical significance of any resulting measurement (for example, the effect of that detection on the measured Sky, its total count, its central position, or any other measurements on the object) will correspondingly decrease to values that are no longer significant in any scientific/statistical measurement and analysis.

6. DISCUSSION

A new method for detecting extremely faint objects and fainter parts of brighter objects in noise is introduced. Unlike the existing approach to detection where the signal is the basis, this approach is based on operations and calculations on the noise with insignificant requirements for the signal. This method is also non-parametric, in other words, it does not involve a functional regression analysis. It is therefore ideal for the study of nebulous/amorphous objects that are heavily immersed in noise, for example, galaxies.

Galaxies can have rich dynamic histories involving internal processes as well as external interactions with the halo or other galaxies. This creates very complicated, diverse morphologies. The fact that we cannot image them in their full 3D glory further complicates their final observed image. Therefore, imposing any a priori model on their shape or radial light profile during the detection process is a self-inflicted systematic bias in their study. Modeling the light profiles of galaxies is vital to our understanding of the galaxies and testing our models, but it should be done *after* detection is complete. Mixing detection and modeling will only bias both.

One major argument in favor of elliptical-based detection and photometry techniques like the Kron and Petrosian radii as opposed to isophotal methods (including NoiseChisel) is that they are impervious to $(1+z)^4$ dimming and K-correction and for any profile, they are “well defined.” By well defined it is meant that if the same galaxy (with the same morphology) exists in multiple redshifts, then such methods will yield the same fraction of total light for all the redshifts. Ideally, when the apertures used extend to infinity (see Graham and Driver 2005), and the galaxies have no morphological evolution, the result would be independent of the noise and thus the threshold used. However, this is not necessarily the case in the real world.

The interpretation of signal-based detection results depends on the morphology of the galaxies under study. To demonstrate this point, consider the simple mean in a 1D distribution as an analogy. Note that the Kron radius is a weighted mean. The mean is a well defined statistic for most distributions because it gives a unique and unambiguous value. Regardless of whether the underlying distribution is a Gaussian or a log-normal distribution, for example, an unambiguous mean can be *defined*, but for *interpreting* the mean, the distributions should not be ignored; otherwise the analysis will be biased when such different distributions are involved.

The same applies to the Kron or Petrosian radii. For any given surface brightness (morphology), a unique and unambiguous radius can be found, rendering them well defined. However, when it comes to interpreting what that radius physically means (in kiloparsecs or fraction of total light, for example), the interpretation will be biased when the morphology (spatial and count distribution of pixels) differs between the sample of galaxies. Therefore, comparing Kron magnitudes for the galaxies of a general population can be problematic. For example, all the galaxies in a (noisy) survey or image which can simultaneously contain irregulars, spirals, and elliptical galaxies.

The Kron or Petrosian radii satisfy the redshift independence in studies of galaxies that are *already known* to have approximately the same morphology; in other words, a morphologically selected sample where the sample has been detected independently of the shape of the galaxies. For example, unlike the references in Section 1, galaxies might indeed have similar morphologies across redshifts (for example, see Lee et al. 2013). However, this claim, or any other claims, including those in Section 1, about the morphology of detected sources can only be tested when the detection technique does not depend on the morphology as an assumption. In other words, if the detection technique depends on galaxies having a similar morphology at similar or various redshifts, it should not come as a surprise if galaxies with similar morphologies are detected.

Isophotal detection methods like NoiseChisel do have the limitation that they use a different threshold for objects at differ-

ent redshifts, or $(1+z)^4$ dimming. However, it should be considered that the Sky value and its standard deviation in the input image are also completely independent of such issues. These vital image statistics, which propagate in all subsequent measurements, only depend on the arriving photons in each pixel regardless of the physical origin of the source. Therefore imposing such high-level (related to physical interpretation and not the data) constraints on low-level measurements (to do with the data, regardless of later physical interpretations) is a source of systematic bias. This noise-based approach to detection was designed to create an accurate low-level measurement tool with as few assumptions as possible so high-level interpretations can be less biased.

High-level interpretations of the outputs of low-level measurements can easily be done after the low-level procedure is complete. For example, to account for $(1+z)^4$ dimming, an individual threshold can be defined based on the measured redshift (a high-level product) for each object in a study. In the 1970s, when the Kron and Petrosian radii were defined, the processing power to achieve this level of customization was not available. Therefore such high-level constraints had to be imposed on the techniques that originated decades ago. However with the very fast computers cheaply available today, there is no more need for such self-inflicted biases.

Through the particular definition of threshold (in Figure 2, Section 3.1.2 and 4.2.1) the cycle of the Sky estimate depending on detection and detection depending on Sky are significantly weakened. In the proposed technique, the detection threshold and initial detection process are defined independently of the Sky value. An independent initial approximation of the Sky is found by averaging the initial undetected regions and is only used in classifying and removing false initial detections (see the flowchart of Figure 2).

Due to all the novel, low-level and non-parametric methods employed in this noise based detection, fainter profiles can be detected more successfully than the existing signal-based detection technique (at least with the parameters used here). The purity measurements of Section 5.2 show how successful this algorithm and its implementation have been in removing false detections, while detecting the very faint true profiles and the fainter parts of large profiles. Section 5.3 then showed the significantly smaller scatter in the photometry of those very diffuse and faint galaxies.

A new approach to segment a detected region into objects that are heavily immersed in noise is also developed. In this approach, the true clumps are first found using the global properties of the noise, not based directly on a user input value or the particular object (compare Section 3.2.1 with Section B.2). By expanding the clumps over the light profile of the detected region, possible objects are found and the detected region is segmented.

One of the design principles of NoiseChisel was to decrease the dependency of the output on user input. To ensure that the results are more dependent on the image than the user’s subjective experience. To achieve this, the true/false criteria were defined based on the image and not an absolute hand input value (see Section 3.1.5 and Section 3.2.1). This approach accounts for local variations in the noise properties or correlated noise that becomes a significant issue in processed data products. Note that by using relative measures the dependence on user input has significantly decreased, but not disappeared.

This noise based approach to detection allows for the input

parameters to require minimal customization between images of different instruments and in different processing stages. For example, in this paper, all the outputs for mock images with ideal noise, raw ground-based images with real noise and *HST/ACS* drizzled space-based images with correlated noise were processed with nearly identical input parameters.

NoiseChisel is designed with efficiency in mind. Therefore it is also very fast in processing a large image. As an example the image of Figure 11 was processed in 4.43 seconds using a 3.06GHz, 4 physical core CPU on a desktop computer. Until now the design and applicability of the concepts introduced here was the primary concern, but in time more efficient algorithms and methods might be found to increase its efficiency. For example including GPU functionality can significantly decrease the running time. The detection and segmentation techniques introduced through NoiseChisel are easily expandable to the detection of any signal in noise, for example, to 3D data in radio studies similar to clumpfind (Williams et al. 1994) and 1D data like spectroscopic data.

The technique proposed here for detection and segmentation along with the ancillary NoiseChisel program provides a fundamentally fresh and new approach to astronomical data analysis. The limited preliminary tests on mock profiles and noise in this paper show that it significantly increases the detection ability, with a reasonable purity and very small photometric scatter, to detect the fainter parts of bright galaxies with any shape or to find small faint objects that will be undetected with the existing signal based approach to detection. Both of these new abilities can play a major role in most branches of galaxy evolution or a astronomy research as whole (some applications are reviewed in Section 1). Along with the new instruments such as *James Webb Space Telescope*, the Large Synoptic Survey Telescope (LSST), and the Thirty Meter Telescope, which will be available in the next few years, this new approach to detection will play a very important role in current and future astronomical discoveries.

ACKNOWLEDGMENTS

We are most grateful to John Silverman for providing very constructive comments and suggestions, particularly on the scientific questions that led to the creation of this technique. Robert Lupton's very critical assessment of this work during several discussions in various stages of its development were very constructive and we are most grateful to him. Anupreet More provided some very critical and useful comments on testing, particularly in Section 5.2. Paul Price kindly supplied us with Figure 11 along with his valuable opinions on this work. Alan Lefor reviewed this text and provided very useful writing style comments for which we are most grateful; he also patiently helped in the initial portability tests of the GNU Astronomy Utilities. The ApJS Scientific Editor (Eric Feigelson) provided valuable comments on the layout and presentation. The critical comments, and references introduced, by the anonymous referee were also very important for the final presentation. Mohammad-reza Khellat, Henry McCracken, Masashi Chiba, Marcin Sawicki, Surhud More, James Gunn, Emanuelle Daddi, Steve Bickerton, and Claire Lackner also provided valuable critical suggestions throughout the duration of this work. M.A. is supported by a Ministry of Education, Culture, Sports, Science and Technology in Japan (MEXT) scholarship. This work has been supported in part by a Grant-in-Aid for Scientific Research (21244012, 24253003)

from MEXT and by the Global Center of Excellence (GCOE), Young Scientist Initiative A.

A. EXISTING SKY CALCULATION METHODS

In existing algorithms for detection, the first step of detection, namely setting a threshold, is based on the Sky value (see Appendix B). To approximate the Sky value prior to detection, researchers use multiple techniques, such as the mode, σ -clipping, etc. A critical analysis of the most common techniques for approximating the Sky value is given here.

A.1. Local Mode

In a symmetric random distribution, for example, pure noise in an astronomical image,¹³ the mean, median, and mode are equal within their statistical errors. With the addition of signal (astronomical objects, yellow histogram in Figure 1), a skewed distribution is formed (red histogram in Figure 1). The mean is the most highly dependent on the skewness since it shifts toward the positive much faster. The median is less affected since it will be smaller than the mean for a given positively skewed distribution. Finally, the mode of the distribution is the least affected statistic of the three. This argument has thus led many to take the mode of a noisy image as the Sky value.

There are several approaches to finding the mode of the image: Bijaoui (1980) finds a functional form to the image histogram in the vicinity of the mode using Bayes's theorem. Kron (1980) finds the mode of the pixel distribution in a 50pixel \times 50pixel (20'' \times 20'') box about the peak of each object based on the mean of the 7 bins in the histogram with the largest number of pixels and considered that as the Sky value. Beard et al. (1990) use a more elaborate approach in the search to find the mode. The histogram is first smoothed with a moving box filter. The highest peaks are found and used in a cubic fit to find the mode which they consider to be the Sky.

DAOPHOT (Stetson 1987) also uses a very similar method: a circular annulus with an inner radius several times the stellar FWHM is taken from a nearby part of the image, sufficiently close to the target and the mode of the pixels in that region is considered as the Sky value. The mode is approximated based on the following relation between the mean and median: $3 \times \text{median} - 2 \times \text{mean}$. This particular relation between the mode, median and mean, can only exist when one assumes a particular pixel count probability distribution function (PDF) or histogram for the image pixels.

SEXtractor can be considered a hybrid, first relying on σ -clipping, and then on finding the mode to find the Sky value. The former will be discussed in Section A.3. In the latter, like DAOPHOT, SEXtractor uses the following relation to find the mode: $2.5 \times \text{median} - 1.5 \times \text{mean}$. In a recent re-analysis of the SDSS stripe 82 (the SDSS deep field), Jiang et al. (2014) use a similar but more accurate hybrid method. The main difference is

¹³ The photon noise actually comes from a Poisson distribution which is not symmetric especially for very low mean (λ) values, but with the very high mean values ($\lambda = B = 10000e^-$ from Figure 1), the Poisson distribution can safely be considered approximately equal to a Gaussian distribution with $\mu = \lambda$ and $\sigma = \sqrt{\lambda}$. Images taken from the *HST* commonly have much smaller Sky values. In such cases, the main source of noise is noise produced by the instrumentation, for example, read-out noise which can out-weight the non-symmetric low- λ Poisson noise.

that they remove SExtractor detections first—with `DETECT_THRESH=2` and `DETECT_MINAREA=4` (see Section B.1). If the mean is not smaller than the median, the mode is assumed to be found based on a similar relation to DAOPHOT between the mean and mode.

Therefore existing methods to use the mode as a proxy for the Sky either employ the parametric approximations of Bijaoui (1980), DAOPHOT, SExtractor, and Jiang et al. (2014) based on an assumed function for the pixel count PDF or a non-parametric one (Kron 1980; Beard et al. 1990). It is clear from Figure 1 that the histogram, which can be considered a binned PDF can take any form of skewness depending on the type and positioning of astronomical data in the image. Therefore by assuming a fixed generic functional form for all possible PDFs, significant systematic errors will be induced.

The existing non-parametric methods reviewed here rely on the image histogram. The results from a histogram depend on the bin-width and the bin positioning, especially in the vicinity of the mode. For example note how the peaks near the mode vary in Figure 20 only due to bin positioning. The method of Kron (1980) for finding the mode (explained above) for the histogram in Figure 1(b.1), yields $4.69e^- \pm 16.02e^-$, where the histogram is made from 200×200 pixels; recall that Kron (1980) used a 50×50 pixels box, and the area here with no signal is much larger than the object. Different bin widths would change this result, but since no generic distribution can be assumed for all images, any generic bin width choice would ultimately be arbitrary. A very accurate, non-parametric method for finding the mode of a distribution that does not rely on the histogram, but on the cumulative frequency plot of the pixels is introduced in Appendix C.

Regardless of how the mode is found, such attempts at using the mode of a distribution as a proxy for the Sky fail to consider the fact that the mode of the distribution also shifts significantly from the actual image background depending on the data that is embedded in the noise. Figure 1 shows that like the mean and median, the mode is a biased estimator for the Sky value due to the data. As the fainter parts of large objects or a large number of faint objects cover a larger fraction of the image, the mode of the distribution shifts to the positive. Figure 1 shows how this shift increases, with mode values of $9.90e^-$ (symmetricity of 1.26, see Appendix C), $9.50e^-$ (0.48) and, $156.10e^-$ (0.44), respectively. Recall that the background value is $0e^-$ in all three. See Section 5.1 for further discussion on the mode as compared to the true Sky.

Reversing the argument above (that data cause a difference between the mode and median), we conclude that if the mode and median are approximately equal, there is no significant contribution of signal or data. In fact this argument is very important for NoiseChisel (see Section 4.2.1). Note that this argument is only possible when the mode is found independently from the median as in Appendix C.

Based on the idea in the previous paragraph we have also created SubtractSky, which is also distributed as part of the GNU Astronomy Utilities. It can be used for cases where only Sky subtraction is desired. Note that the argument above “detects” signal through its effect on the distance of the mode and median, but only based on pixel values and independently of the signal’s spatial distribution. See the manual for more information; its operation is very similar to that explained in Section 4 with small modifications.

A.2. Removing Detections

If the detection algorithm is independent of noise, this method of finding the Sky is the most accurate (see Section 2.2). However, the existing detection algorithms depend on knowing the Sky before they run (see Section B.1). Even so, this method is used by some researchers to find the Sky value, for example, Stoughton et al. (2002) used this technique over a grid to estimate the Sky in the SDSS survey. Bright objects, which are defined as those with at least one pixel above 200σ , are first subtracted from the image. They are all assumed to have power-law wings which are modeled and subtracted from the image and finally a median filter is applied to the image in a box of side $100'' \approx 252$ pixels. Increasing the box size will be a serious burden on the computational process of the pipeline and there will always be objects that are, collectively or individually, large enough to bias the result.

Mandelbaum et al. (2005) reported a systematic decrease in the number of faint galaxies near $< 90''$ of the center of bright objects. It was also observed that this method underestimates the total count of the brighter galaxies (for example, Lauer et al. 2007). The issue was finally addressed in Aihara et al. (2011). The major solution was to change the threshold to detect bright sources to 51σ . Detected objects were deblended, and a linear combination of the best exponential and de Vaucouleurs models were subtracted.

While the decreased threshold and new fitting functions do increase the number of objects that are masked, they still fail in the following respects. (1) Subtraction is done based on parametric model fitting which can potentially be severely wrong in the fainter outer parts of the galaxies that are the primary source of bias. Such cases are when the galaxy cannot be characterized by a simple ellipse or when it is on the edge of the image (see Section B.4). Other cases are when the galaxy might not be a simple $n = 1$ or $n = 4$ profile. (2) The bright and extended objects that do not have a pixel above 51σ are still a cause of systematic bias. For example, none of the bright profiles in Figure 1(c), untruncated) have a pixel above that extremely high threshold. The brightest pixel in Figure 1(c.1) is only 39.67σ above the background.

A.3. σ -clipping

When the outliers of a data set are sufficiently distinct from the majority of the (noisy) distribution, σ -clipping can be very useful in removing their effect. Assuming m is the distribution median, any data point lying beyond $m \pm a\sigma$ can be clipped (removed) and this process can be repeated on the smaller data set n times. The parameters to define σ -clipping can thus be written as (a, n) . Such σ -clipping is only useful if the objects (outliers) have a very high S/N with very sharp boundaries, for example cosmic rays (see Figure 15).

Some prominent uses of this approach in finding the Sky value in an image are: the *HST* image processing pipeline (Gonzaga et al. 2012) with (4, 5) and SDSS Stripe 82 (Annis et al. 2014) with (3, 5) and again (Jiang et al. 2014) with $(_{}^{14}, 20)$. As its primary tool, SExtractor also relies on this approach though the termination criterion is not a fixed number of times, it is the convergence of σ . Asymmetric clipping was proposed by Ratnatunga and Newell (1984). Gonzaga et al. (2012) obtains the

¹⁴ Jiang et al. (2014) do not mention the first parameter.

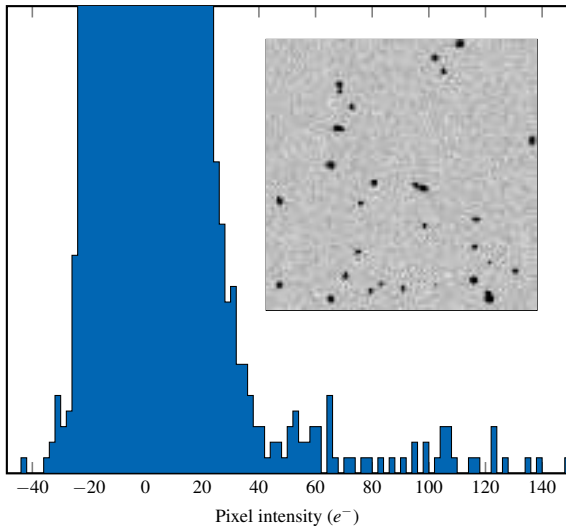


Figure 15: Effect of cosmic rays on the histogram in a small postage stamp (100×100 pixels) of a raw Sky subtracted *HST/ACS* (`flt.fits`) image. The histogram is vertically truncated and the color range in the displayed image has the same range as the histogram. 84 cosmic ray pixels have values above $150e^-$ and are not shown in the histogram. The outlying cosmic rays can easily be distinguished in the histogram due to their sharp boundaries in contrast to the fading boundaries of galaxies, for example, Figure 1(b).

value globally and uses it for the whole image; others use this technique to find the local Sky value and use interpolation over the whole image. The five vertical lines in all three examples of Figure 1 show the position of each iteration’s σ -clipped median with (4, 5) on the mock images. Due to their extreme proximity, they might not be resolved.

Once σ converges, SExtractor uses the mean as the Sky value. For the displayed area of the three examples of Figure 1, the mean, when SExtractor’s convergence is achieved, is, respectively, $11.1 \pm 103.3e^-$, $23.1 \pm 114.2e^-$, and $236.9 \pm 215.6e^-$. Prior to σ -clipping, the median of each image was: $11.1e^-$, $20.2e^-$, and $199.3e^-$. Hence, a simple median (no σ -clipping) was a better approximation to the true background value ($0 \pm 100e^-$). The medians of the (4, 5) σ -clipping technique are shown on Figure 1. It is clear that because the profiles of astronomical objects go slowly into the noise, the correction provided by σ -clipping is very insignificant for the mean and median. For the standard deviation, however, σ -clipping is very useful. The initial standard deviation of these three examples was $167.30e^-$, $455.90e^-$ and $341.05e^-$ (see Section 5.1 for a more complete comparison).

Figure 1 shows how through their very gradual penetration into the noise, stars (the PSF), galaxies, and undetected objects in astronomical images are very different from cosmic rays. Therefore σ -clipping will not suffice when such objects are present. In other words, no matter how much the brightest pixels of objects in an image are clipped, their faint wings penetrate very deep into the noise. Therefore when astronomical objects are present in the image, a generic σ -clip is a very crude overestimation of the Sky value.

A.4. Radius of Flat Profile

Another possible solution to finding the Sky was presented recently as a proxy for the local Sky background behind an object. Barden et al. (2012) has proposed finding the σ -clipped

mean value on elliptical annuli after removing all known source contributions, using SExtractor. As long as the σ -clipped mean is very high above the noise, the slope of the mean pixel value on an annulus as a function of radius will be negative. However, as it approaches the noise, due to the scatter caused by noise, the slope will become repeatedly positive and negative. They consider the position of the second positive to be the annulus on which they find Sky value for each object.

The drawbacks to this method are that it assumes that the profiles can be represented as an ellipse with a well-defined center. It is also based on the Kron radius (Section B.4) which can underestimate the full extent of an object when `DETECT_THRESH > 1` (see Section B.1.2 for a complete discussion). The most important issue with this approach is the area (or number of pixels) which is used to estimate the Sky value. As Stetson (1987) noted, to reach a statistically acceptable precision, the area used to find the Sky value has to be sufficiently larger than the object itself. However, the average value on an annulus is based on a smaller number of pixels than that spanning the parent object especially when all neighboring objects are removed (see their Figure 5). Therefore the random scatter due to the small number of pixels used will limit the ability to measure the true Sky level with accuracy. This is further exacerbated by the fact that the growth of the elliptical annuli is halted based on scatter in the measured Sky of each.

A.5. Median Value of Dithered Images

Median values of dithered images can only be used in images prior to co-adding. This method exploits the dithering, where the field of view of the telescope is shifted slightly between different exposures (for example in Kajisawa et al. 2011). In order to find the Sky value between several temporally close observations, the median pixel value of those observations is taken as the Sky value on each pixel.

The weaknesses of this method are: (1) the Sky value might change between separate observations, particularly in infrared imaging. (2) The main objects in the image have to be far smaller than the dithering length. (3) The field should not be crowded. (4) It assumes perfect bias, dark, and flat fielding since it depends on operations that are done prior to them.

A.6. Background Interpolation

SExtractor and most other algorithms do not find one Sky value for the whole image. Instead, the Sky values are found on a mesh grid. In SExtractor the sizes of the meshes are set to `BACK_SIZE` pixels. It then uses bicubic-spline interpolation to find a the Sky value for each pixel. Figures 16(a)–(c) show SExtractor’s Sky value calculated for each pixel for the three mock images of Figure 1 along with the images in Figures 18 and 19. Recall that the background value for all mock images is zero. It is clear that as the area covered by the faint parts of mock galaxies has increased from (a) to (c) the background values calculated by SExtractor’s σ -clipping and mode approximation have been shifted very strongly to the positive. In this figure the problems with using model based interpolation techniques are also evident. Note how the corners of the images have extremely high and low values compared to the centers of the images in Figure 16 (a)–(c) and (l). Note that the other cases of Figure 16 do not include image corners.

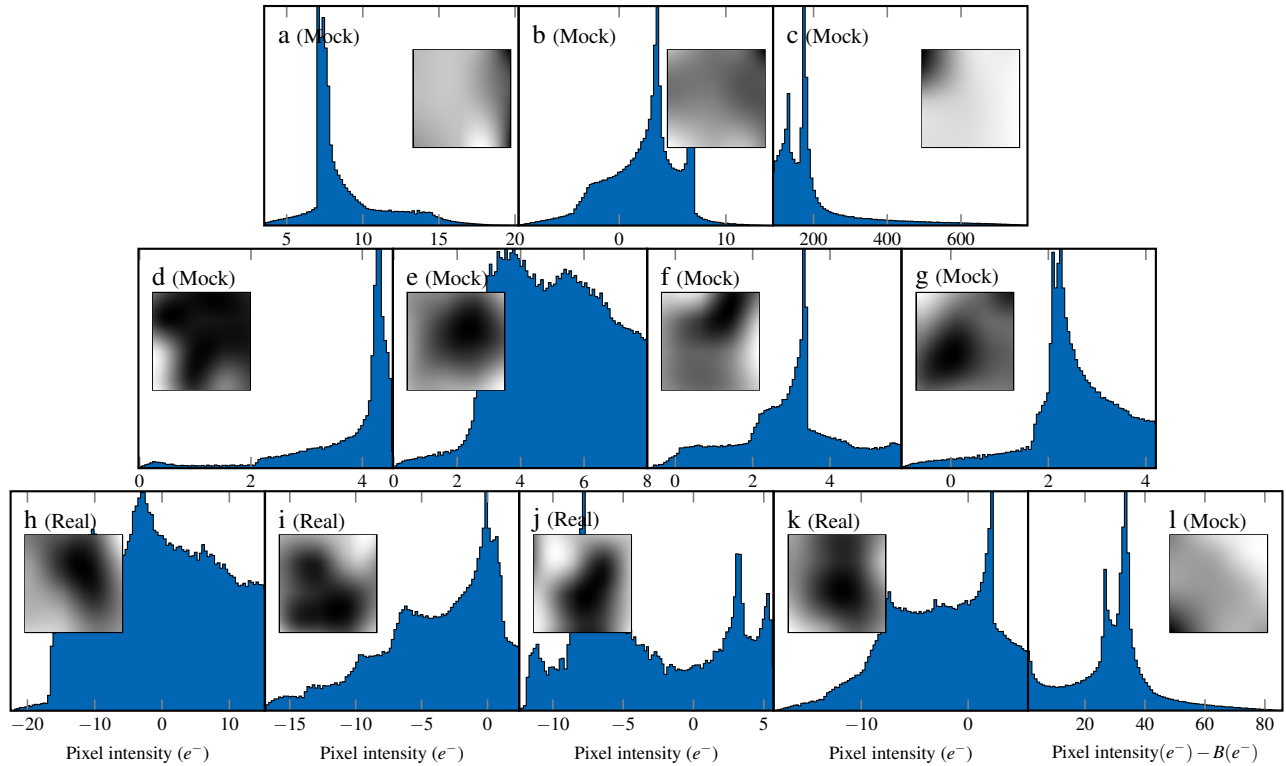


Figure 16: Sky value check images and their histograms, produced by SExtractor with the input parameters of Appendix D applied to the images in some of the figures in this paper. First row (a)–(c): the three mock images of Figure 1. Only for these three, the displayed 200×200 region was input to SExtractor. Second row (d)–(g): the four mock images of Figure 18. Third row: (h)–(l) the four real and one mock image of Figure 19. Failure to interpolate accurately on the corners of the images are clearly visible in (a)–(c) and (l) where the image edge can be seen. Real images are in units of counts s^{-1} , so that the horizontal axis of their histograms are multiplied by $10^5 s$. The true background (B) value of all mock images is subtracted in the histograms.

In SExtractor, through the parameter `BACK_SIZE` (see Appendix D), a user can set a smaller grid on the image. SExtractor then finds the Sky in those sub grids, removes the outliers with median filtering, and interpolates over them. Therefore for each particular image of a particular target, a good choice of `BACK_SIZE` will slightly correct the very large overestimations discussed here. However, for any `BACK_SIZE`, there might be objects in the image that cause a similar or even larger bias. Therefore, unless the best `BACK_SIZE` is found for each particular input image—depending on the objects and their position in the input image—there will be a bias. Such customized application is not practical because of the sheer number of galaxies studied in most papers. If the user chooses a custom background for each image of a large set of targets, comparison between the different images cannot be accurate because of the different statistical properties of the background. Therefore, such significant systematic overestimations will plague any astrophysical analysis or hypothesis testing that is based on them.

B. EXISTING DETECTION AND SEGMENTATION/DEBLENDING METHODS

The detection technique used in astronomy up until now can generally be classified as a signal-based approach with various implementations. It is impractical to review all implementations and their minor differences here. Thus in this appendix we use SExtractor 2.19.5 (Bertin and Arnouts 1996) while mentioning the important alternative implementations during the steps. SExtractor was chosen here because it can easily be installed and has a relatively complete manual. Because of this it is by far the

most commonly used tool by most authors in generating large catalogs or source extraction of known targets and is thus widely recognized by the community. Its techniques are also conceptually very similar and inherited from other packages, for example, DAOPHOT (Stetson 1987), clumpfind (Williams et al. 1994) and Kron (1980).

To extract sources from a noisy image, SExtractor first needs to find the noise characteristics or the Sky value and its error for every pixel. A comprehensive review of the common methods for finding the Sky value are thus provided in Appendix A. Based on the noise, a threshold is applied and regions above noise are chosen as detections (Section B.1). The detections are then deblended (Section B.2). The deblended detections are extended beyond the threshold using the Kron radius concept that is critically analyzed in Section B.4. In Section B.3 a discrete hierarchical Markov image modeling method for simultaneous detection and segmentation of objects in an image is discussed. Since it also requires growing the objects afterwards, it is discussed before Section B.4. The images are outputs of SExtractor. The interpretations of how it has operated are based on its manual or corresponding paper. The configuration file used to run SExtractor is shown in Appendix D.

B.1. Detection

After finding the Sky value, SExtractor uses it to define a threshold (see Section B.1.2). The threshold is applied to a smoothed image (see Section B.1.1). Of the various regions found above the threshold, those with an area smaller than a user defined value are excluded as a false detection (Section B.1.3) and the

remaining objects (true detections) are deblended (Section B.2). Using the Kron (1980) radius concept, the deblended detections are grown on a fixed ellipse to include pixels below the threshold (see Section B.4).

B.1.1. Convolution

A convolution kernel comparable with the PSF has been the best choice for this purpose. A qualitative argument in support of this choice is that it is the widest convolution kernel that can be used such that no object is smoothed out since no object can be smaller than the image PSF (see Bijaoui and Dantel 1970, for a detailed quantitative discussion). Based on this argument, for the example runs of SExtractor on the mock images, the same PSF (Moffat function with $\beta = 4.76$ and FWHM=3 pixels) that was used to create the input image was used. In SExtractor the convolution kernel is specified by the parameter `FILTER_NAME`.

B.1.2. Threshold

In order to detect objects above the noise, a threshold needs to be applied to the convolved image. Only pixels with values above this threshold are considered for object detection. A higher threshold will decrease the probability of false detections, because fewer noise pixels will have a count above it. However, it will miss fainter objects and the fainter parts of brighter objects.

In SExtractor, the threshold is defined in terms of the approximated Sky (s , see Appendix A) and its standard deviation (σ): $s + \text{DETECT_THRESH} \times \sigma$ which are measured on the original input image (prior to convolution). The values set for `DETECT_THRESH` are different in various studies. The recently released 3D-*HST* WFC3-selected Photometric Catalogs in the five CANDELS/3D-*HST* Fields (Skelton et al. 2014) set this parameter to 1.8. In the K_s -selected Catalog in the COSMOS/ULTRAVISTA field (Muzzin et al. 2013), it is set to 1.7. As a final example, in the Subaru/MOIRCS deep survey of the GOODS-N field (Kajisawa et al. 2011), it is set to 1.3.

In order to go deeper in the noise, Rix et al. (2004) proposed a two-stage detection process. In their technique, objects are detected in two runs (values from Rix et al. 2004): (1) a “cold” run where `DETECT_THRESH` is set to a very high value of 2.3, and only the brightest regions of the brightest objects are detected and (2) a “hot” run where it is set to a lower value of 1.65 to detect the fainter objects. The two resulting catalogs are then compared and “hot” objects that lie over the “cold” ones are removed from the final catalog. In their “hot” run, such techniques use the lowest possible threshold they can consider. Working on deeper images, Leauthaud et al. (2007) used 2.2 and 1 for their cold/hot detection thresholds, respectively.

The threshold is calculated based on the original image, but it is applied to the convolved image. Therefore it no longer has the statistical properties that any multiple of the standard deviation is expected to have, for example, that $\sim 95\%$ of the noise pixels have a value below 2σ . This occurs because of the decreased dynamic range after convolution (see Section 3.1.1 and Figure 4). In Figure 4, 1σ , which is the standard deviation of the un-convolved image, corresponds to $100e^-$. However, when applied to the convolved image of Figure 4(b) only 44 (of the 40,000) pixels are above this threshold. Note that the kernel used in Figure 4(b) is the same PSF that was used to make the

mock image. In Figure 4(c)–(e), $100e^-$ far exceeds the brightest convolved pixel.

Based on this idea, Galametz et al. (2013) adopt a different approach to the cold and hot detection technique. `DETECT_THRESH` is approximately similar between the two (0.75 and 0.7), but the convolution kernels (see Section B.1.1) used are significantly different such that the cold run has a much wider kernel (see their Appendix A for the respective SExtractor parameters).

A different approach to finding the threshold of an image, called the “False-Discovery Rate,” was introduced in astronomy by Miller et al. (2001). In this approach the average fraction of false pixel detections to true pixel detections is held fixed when assuming a fixed null hypothesis (background and its noise). It was implemented as a detection technique in Hopkins et al. (2002). All the pixels in the region must be sorted and a p value has to be calculated from an approximated mean and standard deviation. Thus this thresholding technique also needs the Sky and its error prior to the actual detection process.

B.1.3. Detection: True/False

Once the threshold of Section B.1.2 is applied to the smoothed image of Section B.1.1, the image is divided into two groups of pixels: those that are above and below the threshold. The non-white pixels in Figure 17 (a.1)–(d.1) and column 2 in Figures 18 and 19 show this image with a threshold applied (they are all SExtractor’s segmentation maps). In Figure 17, SExtractor is run on the mock image of Figure 1(b.2) with the configuration file of Appendix D. All of SExtractor’s parameters in all four cases are fixed to those in Appendix D except for `DETECT_THRESH`, which is set to 2, 1, 0.5, and 0.1, respectively. The first observation after examining Figure 17 is that as the detection threshold decreases, the number of false detections increases: 0, 0, 319 and 11296, (in the 1000×1000 images, see Section 2.1) respectively.

The major tool available in SExtractor to define and thus remove such false detections is `DETECT_MINAREA`. With this parameter the user can specify the minimum area that a true detection should have. As the threshold decreases, more and more pixels become connected. As an example when `DETECT_THRESH=0.1` is fixed but `DETECT_MINAREA` is set to 10, 25, 50, 75, and 100 pixels, 8989, 3880, 966, 350 and 260 false detections are found. The larger `DETECT_MINAREA` will also result in not being able to detect many compact bright objects that will also be present in a real image. The SExtractor manual therefore correctly suggests setting `DETECT_MINAREA` to small values (1–5) so that the convolution kernel and `DETECT_THRESH` define the sensitivity.

Figure 18 shows the outputs of SExtractor, configured with Appendix D, for extremely faint mock galaxies; see Sections 3.1 and 5.1. SExtractor’s results on a bright and large profile are already analyzed in Figure 17. With `DETECT_THRESH=1`, only the top few pixels of the brightest and sharpest profiles have been successfully detected. Note that as discussed in Section B.1.2, most surveys use much larger thresholds.

When a large S/N for detections is required for accurate fittings, for example, in photometric redshifts or SED fittings, some researchers might opt for discarding such faint detections. However, their detection in the image is nevertheless very important because if they are not detected and removed, they will cause an overestimation in the Sky value, hence systematically underestimating the total count of the brighter, high S/N, objects (see Section 5.1).

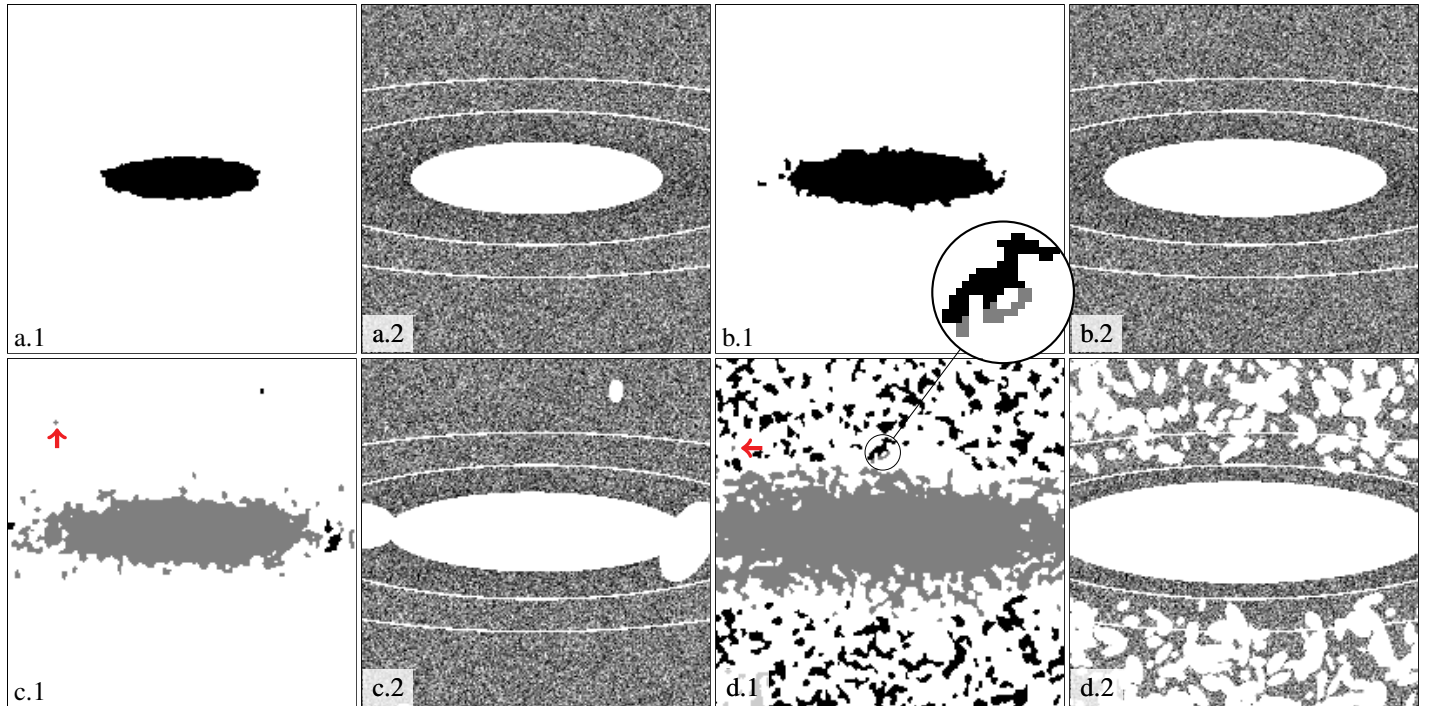


Figure 17: SExtractor results of various thresholds with configuration parameters from Appendix D except for `DETECT_THRESH`. The input image only has the one profile of Figure 1(b) (see Section 2.1). The threshold values for `DETECT_THRESH` are (a) 2, (b) 1, (c) 0.5, (d) 0.1. For each threshold there are two images. Left: the segmentation map. Right: the elliptical region within three times the Kron radius (r_k , see Section B.4) is masked (white) from the original image. Notice the darker profile regions surrounding the elliptical mask that have not been included in the $3, 3r_k$ elliptical aperture. The smaller elliptical border marks the aperture containing $\sim 90\%$ of the counts in the profile. The larger elliptical border shows the region containing $\sim 95\%$ of the counts. The segmentation maps in (c.1) and (d.1) have different color codes for the main object (gray) and any other detections (black). The marked regions show how connectivity is not a criteria in SExtractor’s deblending algorithm.

B.2. Segmentation/Deblending

Segmentation and deblending are defined in Section 3.2. An interesting deblending algorithm is proposed by Lupton (2015) and is employed in the SDSS, Subaru Telescope Hyper Suprime-Cam, and LSST pipelines. In one image (one color) real peaks are defined as those that are at least $3\sigma_{sky}$ above the saddle point or valley that separates it from neighboring peaks in terms of count. True peaks also have to be at least one pixel distant from a neighboring peak. Once the true “child” peaks are found over a detected region, a circular template is built for the child by using the smaller value of two pixels on the opposite sides of the peak. A weight is given to each child and a cost function is defined and minimized to deblend the sources (see Figure 1 of Lupton 2015, for a 1D demonstration).

In choosing a true peak, the area belonging to the peak and the count in it is ignored and a peak pixel is defined as true only if that pixel alone is sufficiently above its immediate valley or saddle point (compare to the discussion in Section 3.2.1). The very important technical issue of how to find the saddle point count is not discussed in that report. One drawback is that this selection criteria will miss real peaks that are below this large threshold but are not due to noise, for example with a very flat profile. In this approach, deblending is completely independent of segmentation. Such pure deblending will also suffer when the detected regions cannot be fitted (the cost function minimized) with the combinations of templates over the detection.

SExtractor uses a concept very similar to contour maps known as *multi-thresholding*. The count range of the detected region is divided into several layers. Then the separate objects in those layers are analyzed and “real” peaks are modeled to find the sep-

arate local maxima and their contribution to the total count (see Figure 2 in Bertin and Arnouts 1996). `clumpfind` (Williams et al. 1994) also uses a very similar approach. Therefore in this approach, first a segmentation map is derived and used to model the objects, and then deblending is done.

In SExtractor’s implementation, a fixed number of layers is defined for all objects, specified by `DEBLEND_NTHRESH` in Section D. Therefore brighter objects, with a very large difference between their peak count and the Sky, will receive layers that are much more widely separated than fainter objects. This will over-segment the fainter objects where the spacing between the layers is less and undersegment the brighter ones. The scale on which the count is divided will also significantly alter the result. In SExtractor, `DETECTION_TYPE` specifies the scale. If set to `CCD`, an exponential scale is used and setting it to `PHOTO` will use a linear scale. Each will output significantly different results.

Once peaks are found between the layers, they are accepted as a true detection or rejected as false based on the parameter `DEBLEND_MINCONT` which specifies the fraction of the total intensity in that peak, or clump, compared to the total, undeblended, detection. Similar to the layer spacing problem mentioned above, this parameter is by definition, biased toward detecting more clumps in fainter objects. Since the threshold to accept a clump differs from one detection to another (based on the total count within each parent detection), a fixed peak will be detected in a fainter object and discarded in a brighter one. Therefore when this selection criteria is adopted for a comparison of clumps in galaxies, added with the layering bias mentioned above, it will bias the results by preferentially detecting more segments (or clumps) in objects with a lower total count before deblending. Another con-

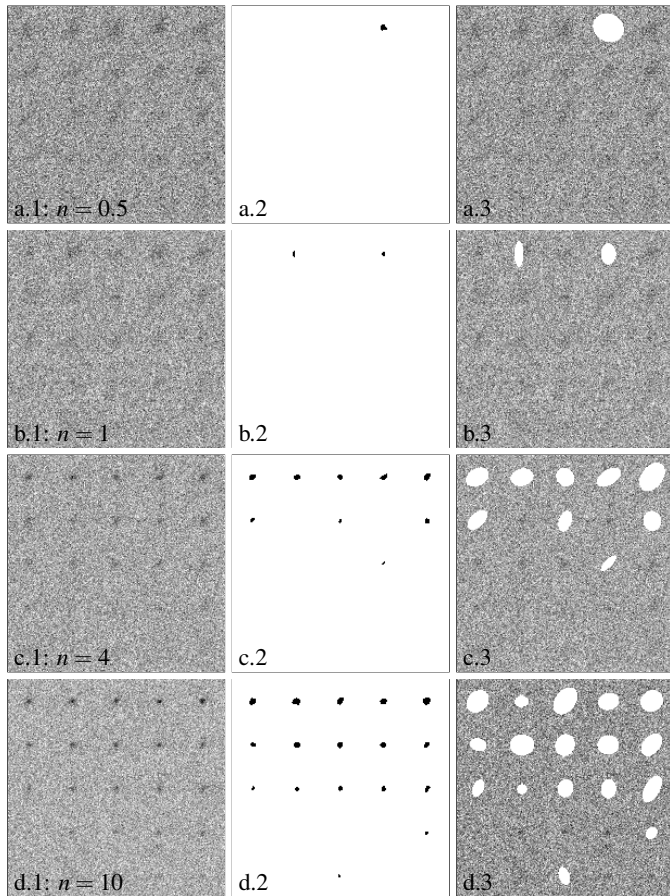


Figure 18: SExtractor sensitivity test. Column 1: the input images, which are the same as those in Figure 12. Column 2: SExtractor’s segmentation maps. Column 3: SExtractor’s detections extended to three times the Kron radius. The SExtractor configuration parameters can be seen in Appendix D.

sequence of this method in finding true clumps is that the result will vary significantly depending on `DETECT_THRESH`. When the threshold is high, the detected total count will be less, and therefore more peaks will be detected in a given object.

The highlighted (magnifying glasses and red arrows) regions in Figure 17 (for mock galaxies) and the large fraction of flagged detections in Figure 19 (for real images) show how SExtractor’s deblending algorithm has failed in the low surface brightness regions. The primary reason for this failure is that SExtractor was designed for high thresholds. When reliable peaks are found (with a high threshold), each pixel is assigned to a peak, assuming all the peaks are a 2D Gaussian far larger than the region above the threshold. This is useful in cases where the peaks’ S/N and the threshold are sufficiently high and all peaks follow a Gaussian profile over the whole image.

In practice, hardly any non-stellar objects of astronomical interest has a Gaussian profile and postage stamps are usually chosen to be larger than the objects in order to get an accurate estimate of the Sky value. Figure 17 shows two ways that SExtractor fails in deblending as the threshold decreases: (1) some of the very far detections of Figure 17(c.1) and (d.1), designated with arrows have been identified as belonging to the main object and (2) a connected region can be shared between two objects that are not physically connected to it as shown in the magnified regions of the same figure. These problems might not cause a significant problem when the magnitude of the very bright mock

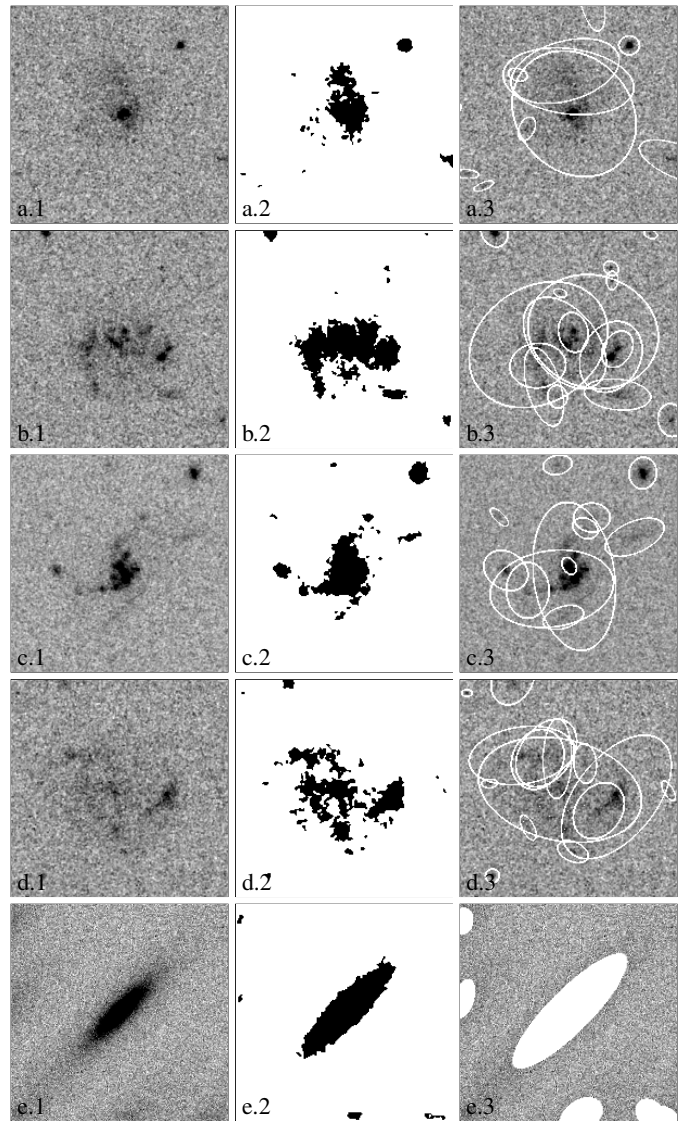


Figure 19: Tests of SExtractor on the same input images as Figure 13. First column: input image. Second column: SExtractor’s segmentation maps. Third column: $3, 3, r_k$ elliptical apertures (see Section B.4). In the real images, because of their complexity, only the borders of the elliptical apertures are shown. In the mock image, the elliptical apertures are filled. Most of the central object detections in a.3, b.3 and d.3 were flagged by SExtractor for possibly biased magnitude measurements.

galaxy in this figure is desired, but when applied to low surface brightness and diffuse galaxies like Figure 19 (a)–(d), very serious systematic errors can be produced.

Figure 19 (a.1)–(d.1) shows SExtractor’s result for the same galaxies in Figure 13. Appendix D shows the configuration parameters used to run SExtractor on these galaxies. The input PSF for these four real galaxies is obtained from the web interface of TinyTim¹⁵ (Krist et al. 2011). The PSF of TinyTim is the theoretical PSF produced on the CCD. In order to create the processed images shown here, various steps of image processing have been applied to these images (see Koekemoer et al. 2007; Massey et al. 2010). Therefore, in practice, the actual PSF on the image

¹⁵ <http://tinytim.stsci.edu/cgi-bin/tinytimweb.cgi>. On Chip 1, pixel position (2047, 1048), filter F814W, Spectrum value 12, PSF diameter $3''$, focus 0.0. SExtractor does not accept kernels larger than 31×31 pixels. Therefore, the central region of this size was cropped from TinyTim’s output for input into SExtractor.

will be slightly different from that produced by TinyTim (see van der Wel et al. 2012). While this difference plays a very important role in model fitting, for the demonstrative purposes on detection here, the TinyTim output is adequate.

It is clear from Figure 19 that the two more diffuse objects in Figure 19(b) and (d) have been deblended into many more separate objects than the two brighter cases of Figure 19 (a) and (c). As explained above, this is due to the inherent biases of SExtractor’s deblending algorithm.

B.3. Combining Detection and Segmentation

A discrete hierarchical Markov image modeling approach was introduced in astronomy recently by Vollmer et al. (2013). This is a fundamentally different approach to detection and segmentation. It is reviewed here because like the more popular methods used today, the detected region needs to be grown to complete the detection as we will discuss next in Section B.4. In this approach object detection and segmentation are done simultaneously. The basic technique comes from image processing applications in particular the quadtree of Laferte et al. (2000).

Hierarchical Markov models have the advantage that they allow to use multi-band images at potentially different pixel resolutions without the need to modify the data as most techniques used in astronomy currently need to do. This makes them “scale free.” However Vollmer et al. (2013) acknowledge that their implementation (MARSIAA) does not account for PSF variation between the inputs. In this approach the problem is labeling of the image pixels “which are spatially connected through a pre-defined neighborhood system. These labels correspond to discrete classes of objects with similar surface brightness” (Vollmer et al. 2013, page 3). Using the multi-band data as input, the procedure iterates along the hierarchies to find a distribution for the labels over the image, see Laferte et al. (2000) for details.

In this approach there is no specific functional basis to do the detection, therefore it is considered as a model-independent detection and segmentation technique. However, instead of known functions, it classifies the image pixels into “classes” which are shared by all the objects in the image. For example, noise has a class of 0 and as the gradient over the object increases, the class also increase; see Figure 9 in Vollmer et al. (2013) for how the class changes toward the center of the object. The number of classes is a free parameter specified by the user. The final simultaneous detection/segmentation depends on the total number of classes and the dynamic range of the image. To detect low surface brightness galaxies, Vollmer et al. (2013) had to truncate or clip the image pixels beyond 20σ , therefore this approach cannot simultaneously detect/segment very bright and very faint objects in one image.

An interesting consequence of this technique is that it does not need to define a count threshold, however, it can only get $\sim 1.5\sigma$ close to the Sky value. Figures 8–10 of Vollmer et al. (2013) show the results of this technique compared to SExtractor’s segmentation maps for three galaxies. In the three cases, the detected area of SExtractor’s segmentation map with a threshold at 1.5σ was comparable or even larger (better covering the objects). This technique heavily relies on iterative processes and thus can be very slow. Vollmer et al. (2013) report it was at least 90 times slower than SExtractor for the same data set.

B.4. Growing Detections Below the Threshold

The high thresholds that were used to avoid false detections cause a very large fraction of the object to not be initially detected (see Figure 17(a.1)–(d.1)). Failing to detect a bright object’s complete area will deprive us of all the valuable information lying hidden there and cause a systematic under- (over-)estimation of the object’s magnitude (Sky value). Therefore when using such large thresholds, it is necessary to use the regions above the threshold as a basis to “grow” the detections and include their fainter parts.

The Kron radius, r_k (Kron 1980), is one of the most popular methods to grow the detection into regions of the image with a count lower than the threshold. It is defined as the light-weighted average radius of a profile,

$$r_k = \frac{\sum rI(r)}{\sum I(r)}.$$

From Figure 17 it is clear that the elliptical parameters and r_k are found based on the region above the threshold, therefore the fainter regions of the galaxies that often harbor valuable information on the dynamical history of the galaxy and might have different morphological parameters cannot be directly measured in the existing signal based approach to detection.

It is generally considered that $2r_k$ contains $\geq 90\%$ of the total count, integrated to infinity (F_I), of a galaxy light profile (see Kron 1980; Infante 1987). Therefore in the literature it is common to use $2.5r_k$ to find the total count of a galaxy. In order to test this claim, SExtractor’s FLUX_AUTO is divided by F_I ¹⁶ for the four different masked $3, 3.r_k$ apertures shown in Figure 17. For this profile, $3, 3.r_k$ contains 74.30%, 78.21%, 80.22% and 87.33% of the total count. The area within the $3, 3.r_k$ has been masked to show the extent of the object that has not been detected. The elliptical apertures containing 90% and 95% of F_I are also shown in Figure 17 for visual comparison.

Graham and Driver (2005) did a thorough analytic study of the mathematical (continuous) 1D Sérsic profile to show how such differences from the expected $> 90\%$ could occur in the calculation of the Kron radius. They showed how dependent the total count within the 2.5 times the Kron radius is to the area that is used to find the Kron radius. If this area is extended to infinity, it is indeed as expected and 2.5 times the Kron radius contains $> 90\%$ of F_I , even for $n = 10$ profiles. However, integration to infinity is not a realistic condition. In practice any measurement of the Kron radius is confined to a certain aperture. By considering the effects of the finite aperture that is used in real measurements of r_k , they show how the values reported above, which have also been reported by other authors are reasonable (see Bernstein et al. 2002; Benítez et al. 2004).

This discussion demonstrates that the statement that an aperture $> 2r_k$ will contain nearly all ($\geq 90\%$) of the light and area of a galaxy is not generic and is only practically correct for very flat profiles. If ignored and used for all galaxies in a survey or image, it can result in a very significant underestimation of the total light and boundaries of the sharper objects, even if it is a pure ellipse as in Figure 17. The underestimation will cause an overestimation in the Sky value of the image, further compounding the resulting systematic bias. The mock galaxy used

¹⁶ F_I is approximated by the total count within $30r_e$. Note that the larger ellipse in Figure 17 which contains 95% of the total light is on $7r_e$.

in this example has a Sérsic index (n) of 4.00, while in the local universe, galaxies with n as large as 11.84 have been reported (Kormendy et al. 2009). The case for distant galaxies becomes much worse, since their apparent r_e in pixels, due to the angular diameter distance, is much smaller with much lower surface brightness.

Figure 18 shows SExtractor’s output for mock galaxies, both flat, low Sérsic index, and sharp or high Sérsic index. Even with `DETECT_THRESH=1`, only a few pixels have been found for each object, the elliptical parameters, namely center, axis ratio, position angle and major axis length (r_k) are all measured using these few pixels. The second argument to `PHOT_AUTOPARAMS` is set to a minimum radius such that if r_k is too small, this minimum radius is used instead of it. This is why most of the ellipses in Figure 18 have similar sizes. However, such hand input values could add more bias to the final result (see Section 5.3 for a discussion on the dispersion of the magnitudes measured in this method).

By definition, r_k depends on finding the full 1D light profile of an object. In order to do that, it is necessary that the center of the profile, its position angle and axis ratio are accurately defined. Furthermore, a good enough sampling of the profile at various (r, θ) is needed in order to approximate the count at a certain radius. These preconditions are only valid in the most optimistic cases, like the bright purely elliptical mock profile of Figure 1(b). In general only a very rare fraction of galaxies display such a simple and bright profile, clearly separated from neighbors or image edges.

Galaxies can have multiple components, for example, the bulge, a bar, and a disk. Each can have a different axis ratio and position angle. The central parts (bulge and a possible bar) are much brighter than the outer disk. Therefore their effect on the overall, light-weighted, estimation of ellipticity will completely outweigh the fainter outer parts, which might not even be detected because of the high thresholds (`DETECT_THRESH>1`) that are commonly used. This compounds the problem mentioned in the previous paragraph for a real galaxy’s total light because all the elliptical parameters in one profile can change in a real galaxy due to their rich dynamical history.

The four real galaxies in Figure 19 visually appear to have a distinct region in the noise. Whether they are composed of separate objects in the same line of sight or are actually one object cannot be judged from one image. In all four examples, because the connectivity of the objects is below the threshold (`DETECT_THRESH=1`), SExtractor considers them to be spatially separated objects. Furthermore, in none of these examples can the connectivity be modeled as a simple ellipse to be able to model.

Figure 19(a.1) appears to have one bright clump and a diffuse host. Because of the relatively flat, diffuse structure, the ellipses showing $3, 3, r_k$ for the three detections have become extremely large. When this happens, the final result is dependent on the accuracy of Sky subtraction, because a large area of sky is also included as part of the object. The large fraction of flagged detections in the real galaxies of Figure 19 shows how `MAG_AUTO` has been flagged as unreliable for most of their sub-components. A user of SExtractor will thus have to either ignore flagged detections or rely on `MAG_ISO`, using only the segmented regions above the threshold. If they choose the latter, for such diffuse objects, `MAG_ISO` is going to miss a very large fraction of the object’s area and photon count.

Due to the sheer number of galaxies that researchers use for

their studies, it is not feasible to check each detection by eye to check when `MAG_AUTO` should be used or `MAG_ISO`. SExtractor does provide `MAG_BEST` to automatically choose between the two, but it is not commonly used in studies today. The main reason is that `MAG_AUTO` and `MAG_ISO` are not consistent and cannot simply be compared with each other in the study of a large number of galaxies.

In Figure 19(e), because of the strong gradient created by bicubic-spline interpolation in SExtractor’s Sky measurement (see Figure 16(1)) no pixel from the the profile on the corner of the image has been detected. Looking at SExtractor’s detections in Figure 19(e.3), it is clear that for such objects, lying on the edges of images, any modeling method of trying to account for their faint regions fails. A very large portion of their total count is left out of their designated Kron aperture. Like the case for clumpy objects, all the necessary requirements to define r_k fail when enough of the object is beyond the edge of an image. Such objects have to be taken into account, particularly if they are the wings of bright objects. While the total magnitude of such objects would always be flagged by software like SExtractor, and not included in any scientific work, failing to account for as much of their light as possible will systematically increase the Sky value that is calculated in such an image. Such cases are common when postage stamp images (for example, Figure 19 (a.1)–(d.1)) of a selected group of galaxies in a larger survey are studied.

The discussions in this section show that the only way to get as close as possible to the “true” total photon count and area of an object of interest is to use lower thresholds. Trying to correct for the photon count which is lost, when a high threshold that is required in the signal-based detection technique is used, will only be a source of systematic bias in measurements and the resulting scientific results. The problems mentioned in this section were the primary motivation in finding a new approach to detection and segmentation that would mitigate many of the problematic issues described above.

C. FINDING THE MODE

In Section A.1, the existing methods to find the mode of an image were reviewed. Here a novel approach to finding the mode of a distribution is proposed. It is very accurate as long as the mode of the distribution is approximately symmetric around it, like the pixel count distributions of Figure 1. This is a safe constraint for images of astronomical targets, which generally have more fainter pixels than brighter ones (the yellow histograms of Figure 1). When the noise is significant, the noise will ensure a symmetric mode similar to the examples of Figure 1. As the signal becomes more significant, the quantile of the mode will shift to lower values.

Given an *ordered* data set X with n elements, where $X_n \geq X_{n-1}$ ($n > 1$). A mirrored distribution is defined about the *mirror* point located at index m as follows. All the data prior to m are placed in opposite order after m , as if a mirror was placed there. The elements of the mirrored data set are thus defined with

$$M_i = \begin{cases} X_i & i \leq m \\ X_m + (X_m - X_{m-(i-m)}) & i > m \end{cases}$$

The mirrored distribution is therefore identical to the original distribution until and including X_m . M has $2(m-1) + 1$ elements and like X , it is ordered. Figure 20 shows one example

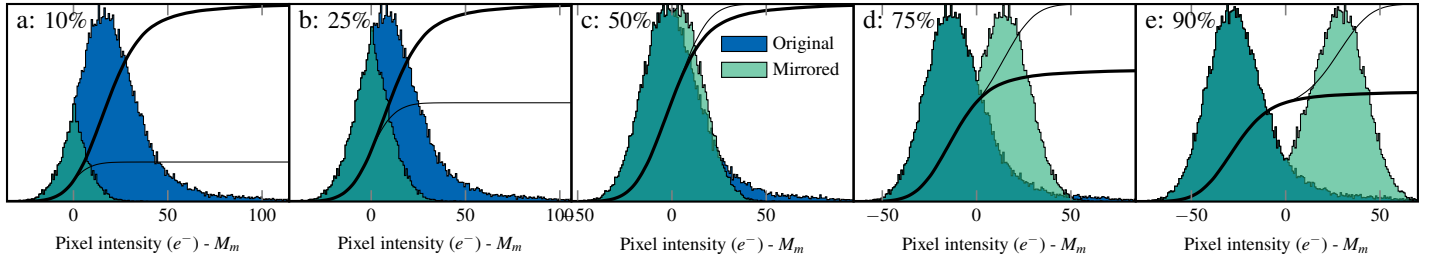


Figure 20: Mirrored distribution compared with the original distribution. The data set is the pixels of Figure 9(b.2) multiplied by 10^4 seconds. M_m is the value on the mirror point. Blue and green histograms are the histograms of the original and mirrored distributions, respectively. The thick and thin lines are the cumulative frequency plots of the original and mirrored distributions, respectively. The percentage value shown after the label of each plot shows the percentile of the original distribution on which the mirror was placed. It is clear that as the mirror point gets closer to the mode of the distribution, the two lines diverge more smoothly. The cumulative frequency curve is scaled to the tip of the blue histogram.

data set (the pixels of Figure 9(b.2)) with mirrored distributions overplotted. The mirror points in Figure 20 are placed at various quantiles of the original distribution in each case. The histogram is only displayed in this demonstration to aid the understanding. It is not used at all during the analysis.

Figure 20 shows that when the mirror is very far from the mode, the cumulative frequency plot of the mirrored distribution will deviate below or above that of the original pixels very sharply. As the mirror approaches the mode, the maximum difference of the two cumulative frequency plots in the vicinity of the mode becomes smaller. Therefore, on the symmetric mode of a distribution, the two cumulative frequency plots should remain very similar for a large number of pixels (or distance in the ordered array) after the mirror.

Let $\delta(M_i, m)$ represent the difference between the cumulative frequency plots of the original and mirrored data sets for M_i , when the mirror is placed on the index m . For any given mirror position and positive integer N , let $\Delta(m)$ be the maximum $|\delta(M_i, m)|$ for all $m < i < m + N$. Then the symmetric mode of a distribution can be found by finding m such that $\Delta(m)$ is minimized. The Golden section search algorithm (Kiefer 1953) is used to find the mirror point that minimizes $\Delta(m)$.

If the distribution has several symmetric local maximums, and as long as N is large enough, the first (with the lowest quantile) will be found, even if the brighter peak has more pixels in its proximity (see Figure 21(c) for a distribution with two local maximums in the histogram). This is exactly what is desired in astronomical image processing because if there is a second local maximum with a larger count and larger number of pixels, then that local maximum is not due to noise. Noise will always produce the first (lowest count) local maximum, which can be called the *mode*. In most astronomical applications of low S/N objects, the first local maximum will be the only one. If not, it will have more pixels in its vicinity than any other local maximum in the pixel distribution.

The mirror cumulative frequency plot found for the mode should be approximately equal to the actual data in the vicinity of the mode. Beyond that, it should ideally always remain below the actual data (see Figure 21). However, in minimizing $\Delta(m)$ as defined above, the resulting mirror cumulative frequency plot will zig-zag around the actual distribution since $|\delta(M_i, m)|$ was used. The cumulative frequency plot is fundamentally a counting function. Therefore, the error in choosing an index, say m , follows a Poisson distribution. Thus the standard deviation in finding m is \sqrt{m} . Hence a limit can be set on how negative $\delta(M_i, m)$ can become. Taking α to be a given constant specified by the user, if $\delta(M_i, m) < -\alpha\sqrt{m}$, $\Delta(m)$ is set to a fixed

constant, let's call it C .¹⁷ The golden section search is modified from its standard algorithm to choose the interval with the lowest values when it confronts C . Recall that such conditions only occur when m is a significant overestimation of the mode.

Figure 21(a) shows the result for the same distribution of Figure 20. In Figure 21(b) this technique is applied to the more skewed distribution of the convolved image of Figure 10(c.1). A very bright spiral galaxy has caused the postage stamp pixel distribution to be more skewed. Figures 21(c) and (d) show the distributions of two mock images with two very bright and large Sérsic profiles of $n = 2.5$ and $n = 0.5$ placed in a small postage stamp respectively. These are two extreme cases, showing how the quantile of the mode can reach extremely low quantiles.

As the distribution becomes more skewed, the mode shifts to lower quantiles; see Figure 21. This is the basis of the new method to define the threshold of the image (explained fully in Section 3.1.2 and Section 4.2.1). In these examples, the boundaries for the golden section search are set to the 0.01 and 0.51 quantiles of the image. As long as data is present in the image (which create a positive skew) the mode will not exceed the median, thus the higher limit. In these examples, N is set to be $1/2$ of the total number of pixels and in order to be more efficient, $\delta(M_i, m)$ is sampled in 1000 equally spaced points between M_m and M_{m+N} . α is also taken to be 1.5.

Depending on the brightness of the data pixels and the fraction of pixels that they occupy, the mode calculated with this technique can lose its accuracy or it can cease to exist. Also, in extremely skewed distributions, the golden section intervals might miss the mode and converge on a lower mirror point. Therefore a measure of quality is necessary to accompany the mode.

Let a be the value of the 0.01 quantile of the mirrored distribution. The minimum is not chosen due to its scatter. Take b to be the value on the mode and finally, let c be the value of the first M_i beyond the mode where $|\delta(M_i, m)| > \alpha\sqrt{m}$, same α as above. This point is marked on the plots of Figure 21 with a dotted vertical line. These three values can define a measure of “symmetricity” (s) about the mode with:

$$s = \frac{c - b}{b - a}$$

The symmetricity for the examples of Figure 21 are respectively: 0.43, 0.25, 0.84 and 0.74. Based on these and other simulations, $s > 0.2$ appears to be a good symmetricity of an accurate

¹⁷ The value of C is an internal issue and is irrelevant to this discussion or the user. It is only necessary that it should be larger than the largest possible $\Delta(m)$.

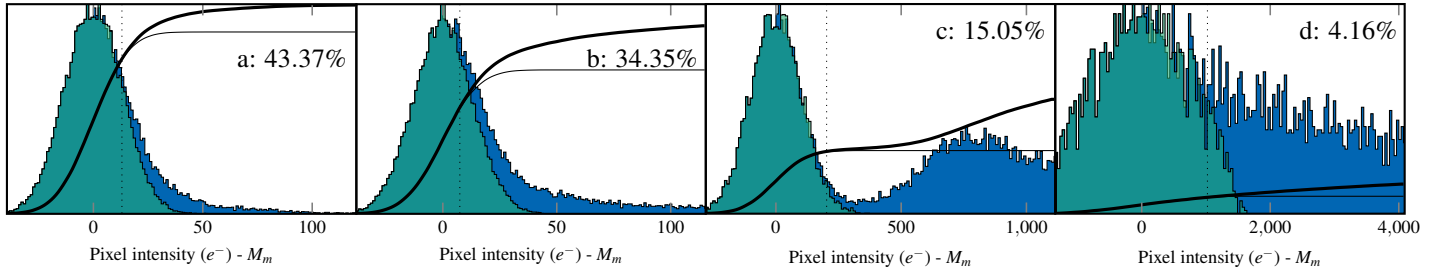


Figure 21: Finding the mode by minimizing $\Delta(m)$. Similar to Figure 20, with the mirror placed on the mode. The dotted line shows the first value where $|\delta(M_i, m)| > 1.5 \sqrt{m}$, which is used to find the “symmetricity” of the mode (see text). (a) Same data set as Figure 20. (b) The convolved image of Figure 10(c.1): a bright and large galaxy skewing the distribution, further shifting the mode to lower percentiles. (c) The convolved and noisy image of a circular -20 magnitude mock Sérsic profile with $n = 2.5$, $r_e = 50$ pixels, truncated at $2r_e$ with center on (100, 140) in a 200×200 pixel image. (d) Similar to (c) but -28 magnitude with $n = 0.5$, $r_e = 100$, truncated at $5r_e$ placed at (110, 285).

“symmetric” mode, when the mode is above the ~ 0.02 quantile of the image. When the output mode approaches such quantiles, $b - a$ in the equation above will be too small to give an accurate result.

In addition to the initial cost of sorting of the data set, the rest of the process is very simple and not CPU intensive, since only 1000 points are checked in each round of the golden section search. Therefore the CPU cost of running this technique is similar with the cost for σ -clipping which also requires sorting, to find the median, but needs multiple passes through the whole data.

D. SEXTRACTOR PARAMETERS

Below is a list of the SExtractor parameters used in this study. We make no claim that these are “the best” (or worst) possible set of parameters. The values for each parameter were selected based on values reported by other research teams which extensively used SExtractor in their astrophysical data analysis and its manual; see Appendices A and B.

The file `PSF.conv` refers to the PSF used to create mock images when SExtractor was applied to the mock images and to that produced by TinyTim when real *HST* images were used; see Appendix B for more details.

```
MEMORY_OBJSTACK 3000
MEMORY_PIXSTACK 300000
MEMORY_BUFSIZE 1024
```

```
DETECT_TYPE CCD
GAIN_KEY GAIN
PIXEL_SCALE 1.0
FITS_UNSIGNED N
```

```
BACK_TYPE AUTO
BACK_SIZE 64
BACK_FILTERSIZE 3
BACKPHOTO_TYPE LOCAL
BACKPHOTO_THICK 24
```

```
WEIGHT_TYPE BACKGROUND
WEIGHT_GAIN N
```

```
FILTER Y
FILTER_NAME PSF.conv
MASK_TYPE CORRECT
```

```
INTERP_MAXLAG 16
INTERP_MAXLAG 16
INTERP_TYPE ALL
```

```
DETECT_THRESH 1
ANALYSIS_THRESH 1
THRESH_TYPE RELATIVE
DETECT_MINAREA 5
```

```
DEBLEND_NTHRESH 64
DEBLEND_MINCONT 0.001
CLEAN Y
CLEAN_PARAM 1.5
```

```
FLAG_IMAGE flag.fits
FLAG_TYPE OR
```

```
SEEING_FWHM 1.2
STARNNW_NAME default.nnw
```

```
MAG_ZEROPOINT 0.0
PHOT_APERTURES 5
PHOT_AUTOPARAMS 3,3.5
PHOT_AUTOAPERS 0,0
PHOT_FLUXFRAC 0.5
PHOT_PETROPARAMS 2.0,3.5
SATUR_LEVEL 50000.0
SATUR_KEY SATURATE
```

```
CHECKIMAGE_TYPE SEGMENTATION,APERTURES,BACKGROUND
CHECKIMAGE_NAME seg.fits,aper.fits,back.fits
```

```
CATALOG_NAME SResults.txt
CATALOG_TYPE ASCII_HEAD
PARAMETERS_NAME ./parameters/sextractor/sextractor.param
```

```
VERBOSE_TYPE NORMAL
```

E. NOISECHISEL PARAMETERS

The full list of parameters that was used for NoiseChisel in this paper is printed here. If a different parameter was used, it is explained in the text. Note that we do not consider these parameters to be “the best” for any generic data set. For the processing of Figure 11, `--nch1=4`, `--lmesh=256` and the following two on/off options were also activated `--fullinterpolation` and `--fullsmooth`. For the *HST* images, `--skysubtracted` was activated.

```
# Input:
hdu 0
khdu 0
skysubtracted 0
minfrac 0.5
```

```

minnumfalse      100
# Mesh grid:
smeshsize        32
lmeshsize        200
nchl              1
nch2             1
lastmeshfrac     0.51
mirrordist       1.5
minmodeq         0.49
numnearest       10
smoothwidth      3
fullconvolution  0
fullinterpolation 0
fullsmooth       0
# Detection:
qthresh          0.3
erode            2
erodengb         4
opening          1
openinggb        8
sigclipmultip    3
sigcliptolerance 0.2
dthresh          -0.1
detsnminarea     15
detsnhistnbins  0
detquant         0.99
dilate           3
# Segmentation:
segsnminarea     25
segquant         0.99
segsnhistnbins  0
gthresh         0.5
minriverlength   15
objbordersn      1

```

Irwin, M. J. (June 1985). *MNRAS*, 214, 575

Jiang, L. et al. (July 2014). *ApJS*, 213, 12

Kajisawa, M. et al. (Nov. 2010). *ApJ*, 723, 129

Kajisawa, M. et al. (Mar. 2011). *PASJ*, 63, 379

Kauffmann, G., S. D. M. White, and B. Guiderdoni (Sept. 1993). *MNRAS*, 264, 201

Kennicutt Jr., R. C. (Sept. 1989). *ApJ*, 344, 685

Kiefer, J. (1953). *Proc. Amer. Math. Soc.* 4, 502

Klypin, A., A. V. Kravtsov, O. Valenzuela, and F. Prada (Sept. 1999). *ApJ*, 522, 82

Koekemoer, A. M. et al. (Sept. 2007). *ApJS*, 172, 196

Kormendy, J., D. B. Fisher, M. E. Cornell, and R. Bender (May 2009). *ApJS*, 182, 216

Kregel, M. and P. C. van der Kruit (Nov. 2004). *MNRAS*, 355, 143

Krist, J. E., R. N. Hook, and F. Stoehr (Oct. 2011). *Proc. SPIE*, 8127,

Kron, R. G. (June 1980). *ApJS*, 43, 305

Lackner, C. N. and J. E. Gunn (Apr. 2012). *MNRAS*, 421, 2277

Laferte, J.-M., P. Perez, and F. Heitz (Mar. 2000). *ITIP*, 9, 390

Lauer, T. R. et al. (June 2007). *ApJ*, 662, 808

Leauthaud, A. et al. (Sept. 2007). *ApJS*, 172, 219

Lee, B. et al. (Sept. 2013). *ApJ*, 774, 47

Lotz, J. M. et al. (Jan. 2006). *ApJ*, 636, 592

Lundgren, B. F. et al. (Jan. 2014). *ApJ*, 780, 34

Lupton, R. H. (Aug. 2015). *Personal home page*,

Lupton, R. H., J. E. Gunn, and A. S. Szalay (Sept. 1999). *AJ*, 118, 1406

Macciò, A. V. et al. (Mar. 2010). *MNRAS*, 402, 1995

Mandelbaum, R. et al. (Aug. 2005). *MNRAS*, 361, 1287

Massey, R. et al. (Jan. 2010). *MNRAS*, 401, 371

McLean, I. S. (2008). 2nd. Praxis Publishing Ltd. ISBN: 978-3-540-76582-0.

Miller, C. J. et al. (Dec. 2001). *AJ*, 122, 3492

Miyazaki, S. et al. (Dec. 2002). *PASJ*, 54, 833

Murata, K. L. et al. (May 2014). *ApJ*, 786, 15

Muzzin, A. et al. (May 2013). *ApJS*, 206, 8

Perret, B., S. Lefèvre, and Ch. Collet (2009). *Pattern Recognition*, 42, 2470

Petrosian, V. (Oct. 1976). *ApJ*, 209, L1

Pohlen, M. and I. Trujillo (Aug. 2006). *A&A*, 454, 759

Presotto, V. et al. (May 2014). *A&A*, 565, 126

Ratnatunga, K. U. and E. B. Newell (Jan. 1984). *AJ*, 89, 176

Rix, H.-W. et al. (June 2004). *ApJS*, 152, 163

Scoville, N. et al. (Sept. 2007). *ApJS*, 172, 1

Sérsic, J. L. (1963). *BAAA*, 6, 41

Skelton, R. E. et al. (Oct. 2014). *ApJS*, 214, 24

Starck, J. and F. Murtagh (2006). 2nd. Springer. ISBN: 978-3-662-04908-2.

Stetson, P. B. (Mar. 1987). *PASP*, 99, 191

Stoughton, C. et al. (Jan. 2002). *AJ*, 123, 485

van der Wel, A. et al. (Dec. 2012). *ApJS*, 203, 24

van Dokkum, P. G. (Nov. 2001). *PASP*, 113, 1420

van Dokkum, P. G. et al. (Jan. 2015). *ApJ*, 798, 45

Vincent, L. and P. Soille (June 1991). *ITPAM*, 13, 583

Vollmer, B. et al. (Feb. 2013). *AJ*, 145, 36

Williams, J. P., E. J. de Geus, and L. Blitz (June 1994). *ApJ*, 428, 693

REFERENCES

Abraham, R. G. and P. G. van Dokkum (Jan. 2014). *PASP*, 126, 55

Abraham, R. G. et al. (Nov. 1996). *ApJS*, 107, 1

Aihara, H. et al. (Apr. 2011). *ApJS*, 193, 29

Annis, J. et al. (Oct. 2014). *ApJ*, 794, 120

Anscombe, F. J. (Feb. 1973). *The American Statistician*, 27, 17

Barden, M. et al. (May 2012). *MNRAS*, 422, 449

Beard, S. M., H. T. MacGillivray, and P. F. Thanisch (Nov. 1990). *MNRAS*, 247, 311

Benítez, N. et al. (Jan. 2004). *ApJS*, 150, 1

Bernstein, R. A., W. L. Freedman, and B. F. Madore (May 2002). *ApJ*, 571, 56

Bertin, E. and S. Arnouts (June 1996). *A&AS*, 117, 393

Bijaoui, A. (Apr. 1980). *A&A*, 84, 81

Bijaoui, A. and M. Dantel (May 1970). *A&A*, 6, 51

Cayón, L., J. Jin, and A. Treaster (Sept. 2005). *MNRAS*, 362, 826

Chandola, V., A. Banerjee, and V. Kumar (July 2009). *ACM Comput. Surv.* 41, 15:1

Cowie, L. L., E. M. Hu, and A. Songaila (Oct. 1995). *AJ*, 110, 1576

de Grijs, R., M. Kregel, and K. H. Wesson (July 2001). *MNRAS*, 324, 1074

de Vaucouleurs, G. (1959). *Handbuch der Physik*, 53, 275

Donoho, D. and J. Jin (2004). *The annals of Statistics*, 32, 962

Dougherty, E. (1992). 1st. CRC Press. ISBN: 9780824787240.

Ellison, S. L., J. T. Mendel, D. R. Patton, and J. M. Scudder (Nov. 2013). *MNRAS*, 435, 3627

Elmegreen, D. M., B. G. Elmegreen, S. Ravindranath, and D. A. Coe (Apr. 2007). *ApJ*, 658, 763

Galametz, A. et al. (June 2013). *ApJS*, 206, 10

Gonzaga, S., W. Hack, A. Fruchter, and J. Mack (June 2012).

Gonzalez, R. C. and R.E. Woods (2008). 3rd. Prentice Hall. ISBN: 978-0131687288.

Graham, A. W. and S. P. Driver (2005). *PASA*, 22, 118

Hawkins, D. M. (1980). Chapman & Hall. ISBN: 978-94-015-3996-8.

Hopkins, A. M. and J. F. Beacom (Nov. 2006). *ApJ*, 651, 142

Hopkins, A. M. et al. (Feb. 2002). *AJ*, 123, 1086

Illingworth, G. D. et al. (Nov. 2013). *ApJS*, 209, 6

Infante, L. (Sept. 1987). *A&A*, 183, 177